

Computational 3D Modelling of Electric Fields in Fingrid Oyj's Electrical Grid

Tuukka Lehtinen

School of Electrical Engineering

Thesis submitted for examination for the degree of Master of Science in Technology.

Espoo 31.10.2017

Thesis supervisor:

Prof. Ilkka Laakso

Thesis advisors:

M.Sc. Juhani Tonteri

Prof. Ilkka Laakso

Author: Tuukka Lehtinen

Title: Computational 3D Modelling of Electric Fields in Fingrid Oyj's Electrical Grid

Date: 31.10.2017

Language: English

Number of pages: 6+58

Department of Electrical Engineering and Automation

Professorship: Electromagnetics in Health Technologies

Supervisor: Prof. Ilkka Laakso

Advisors: M.Sc. Juhani Tonteri, Prof. Ilkka Laakso

In this thesis, extremely low frequency external electric fields as well as fields induced into a human body are simulated in various occupational exposure scenarios. The simulated environment is a Fingrid Oyj operated electrical substation. A realistic 3D model of a section of the substation is created and simulations are conducted using software implemented in MATLAB. The software solves the electric fields using finite element method. The human body being exposed to the external electric field is portrayed by a voxel based human phantom model.

The results received from the simulations are compared with 2013/35/EU directive safety limits to verify safe working conditions at the studied site. Additionally, the simulated results are compared with data obtained from experimental measurements. This comparison is done to both validate the simulation results and to confirm that the calculations and equations used in conjunction with the experimental measurements produce reliable results.

The results obtained show that the EU directive safety limits are not exceeded in the studied occupational scenarios and that the experimental measurement methods previously used by Fingrid work as intended in the majority of cases.

Keywords: ELF electric fields, Electric field exposure, Computational dosimetry

Tekijä: Tuukka Lehtinen

Työn nimi: Sähkökenttien laskennallinen 3D mallintaminen Fingrid Oyj:n sähköverkossa

Päivämäärä: 31.10.2017

Kieli: Englanti

Sivumäärä: 6+58

Sähkötekniikan ja automaation laitos

Professori: Sähkömagnetiikka terveysteknologioissa

Työn valvoja: Prof. Ilkka Laakso

Työn ohjaajat: M.Sc. Juhani Tonteri, Prof. Ilkka Laakso

Tässä diplomityössä mallinnetaan matalataajuuksisia ulkoisia sähkökenttiä, sekä ihmiskehoon indusoituvia sisäisiä sähkökenttiä ammatillisessa työskentely-ympäristössä sähköasemalla. Simulaatiokohteena toimivasta Fingrid Oyj:n ylläpitämästä sähköasemasta tehtiin 3D-malli, jossa sähkökenttiä simuloitiin MATLAB-ohjelmiston avulla. Sähkökenttien ratkaisemiseen ohjelmisto käyttää elementtimenetelmää. Sähkökenttäaltistuksen kohteena toimi vokselipohjainen ihmiskehomalli.

Simulaatioista saatuja tuloksia verrataan 2013/35/EU direktiivin sähkökenttien turvarajoihin, jotta saadaan varmuus työskentelyolosuhteiden turvallisuudesta tutkimuskohteessa. Simulaatiotuloksia verrataan lisäksi kokeellisissa mittauksissa saatuihin tuloksiin. Vertaus kokeellisiin mittaustuloksiin tehdään simulointitulosten vahvistamiseksi, sekä kokeellisissa mittauksissa käytettyjen laskujen ja kaavojen toimivuuden varmistamiseksi.

Simulaatioiden tulokset osoittavat, että EU direktiivin turvarajat sähkökentille eivät ylity tutkitussa kohteessa ja Fingridin aikaisemmin käyttämät kokeelliset mittausten menetelmät toimivat oletetusti valtaosassa tapauksista.

Avainsanat: Matalataajuuksiset sähkökentät, Altistuminen sähkökentille, Laskennallinen dosimetria

Preface

I would like to express my sincere gratitude for the guidance and insight Professor Ilkka Laakso has provided me throughout this thesis work. I also want to thank the group of people at Fingrid with whom I had the chance to work with, especially my instructor Juhani Tonteri.

Otaniemi, 31.10.2017

Tuukka Lehtinen

Contents

Abstract	ii
Abstract (in Finnish)	iii
Preface	iv
Contents	v
Symbols and abbreviations	vi
1 Introduction	1
2 Background	2
3 Methods	9
4 Validation of Methods	25
5 Results	33
6 Conclusions	52
References	54

Symbols and abbreviations

Symbols

B	magnetic flux density
D	electric flux density
E	electric field strength
H	magnetic field strength
I	current
J	current density
N	depolarization factor
p	perimeter
Q	electric charge
U	electric potential
ε	permittivity
ε_r	relative permittivity
ε_0	permittivity of vacuum
ρ	charge density
σ	electric conductivity
ϕ	scalar potential

Operators

$\nabla \cdot \mathbf{A}$	divergence of vector in \mathbf{A}
$\nabla \times \mathbf{A}$	curl of vector in \mathbf{A}
$\frac{\partial}{\partial t}$	partial derivative with respect to variable t

Abbreviations

AC	alternating current
AL	action level
CAD	computer-aided design
CNS	central nervous system
ELF	extremely low frequency
ELV	exposure limit value
EMF	electromagnetic field
EU	European Union
ICNIRP	International Commission on Non-Ionizing Radiation Protection
RMS	root mean square
SAR	specific absorption rate

1 Introduction

The Finnish national electricity transmission grid operator Fingrid Oyj operates and maintains the Finnish main electric grid. Fingrid operates an infrastructure consisting of 110, 220 and 400 kV power lines, over hundred electrical substations and a few reserve power plants. Occupational work at facilities like these is strictly regulated for the safety of workers. One aspect of the regulation is exposure to electromagnetic fields. Exposure to these fields is regulated by a law of the Finnish Council of State, which implements a European Union (EU) directive. The directive obliges the employer to demonstrate that working conditions are safe by performing field exposure measurements and calculations. Fingrid has previously fulfilled all obligations set by the EU directive and have demonstrated that the directive safety limits are not exceeded. This has been done by performing a set of experimental measurements using a helmet-mask measurement system. However, when the EU directive for electromagnetic field exposure was update with a new way of defining safety limits using induced electrical field strengths instead of induced current densities in 2013, there was a call to update Fingrid's previous studies as well. Since the enforcement of the new directive Fingrid has developed a novel method of converting results of their previous studies to match the newly defined standard. This thesis aims to verify that the newly developed conversion method functions reliably.

The main goal of this thesis work is to repeat a set of experimental measurements and calculations previously conducted by Fingrid and to reproduce these scenarios using computational simulations. The results of the experimental measurements are cross-checked against the simulations. This comparison is done to verify that the helmet-mask measurement system produces reliable results and that the conversion between the new and old EU limits works. A 400kV electric substation, specifically the surroundings of two side by side circuit breakers operating at the same phase of alternating current was chosen as the measurement and simulation location. This specific location was chosen because previous studies indicate that the strongest external field strengths occur at locations similar to this. Hence, if the EU directive safety limits are not exceeded at this location, deductions of the safety at other locations can also be made. A secondary goal of the thesis is to generally map and visualize the external electric fields surrounding the circuit breakers as well as the electric fields being induced into a human body while exposed to the external field.

This thesis work is divided into five sections: A background section, where the 2013 EU directive and its safety limits are presented, a look into the previous studies concluded by Fingrid is taken and the state of research on extremely low frequency electric field dosimetry is analysed. The second section covers the methods used throughout the work. This includes descriptions of the experimental measurements, the modelling of the simulation geometry, the human model used as well as an explanation on how the simulation algorithm functions. The third section is dedicated to the validation of the chosen methods and to explaining the design choices made. In the fourth section results for both the experimental measurements and for the computational simulations are presented. Finally, the fifth chapter summarizes the end results and discusses their implications.

2 Background

In this literature review chapter, the 2013/35/EU directive [1] on occupational health, and safety requirements for electric and magnetic field exposure are introduced. Additionally, health effects of exposure to electric fields are discussed. Also covered is, how these guidelines affect the operations of Fingrid and what the company has already done to study and ensure compliance with these new regulations. Lastly, an in-depth look at the research already conducted on the modelling of extremely low frequency (ELF) electric field exposure is taken.

EU directive

As previously noted the European Parliament and council enacted a new directive in 2013 on the health and safety requirements for work done in proximity to strong electromagnetic fields (EMF). This new directive replaces an older directive from 2004 [2] and its intention is to guarantee safe working conditions for employees working in the EU. The directive concentrates only on acute health and safety risks caused by time-varying and static electromagnetic fields. Long-term effects of exposure to electromagnetic fields are not covered. This is mainly due to the lack of conclusive scientific evidence, establishing a causal relationship between long-term exposure to electromagnetic fields and health effects.

The actual way the directive endeavours to assure safe working conditions is by imposing safety limits for exposure. The directive imposes four different safety values for electric fields: Two “action levels” values (ALs): Low ALs and high ALs which declare maximum strength for the external electric field in the working environment, the difference being that the higher safety limit allows slightly higher exposure if proper precautions are taken; and two “exposure limit values” (ELVs), which define what magnitude electric fields induced into the human body cause harmful health and sensory effects. The ALs are declared as RMS values and the ELVs as temporal peak electric field strength values in V/m. It is also noteworthy that the exposure limits are frequency dependent and in our case the relevant frequency is the 50 Hz power line frequency. The ALs and ELVs are shown in table 1. The ELVs for health effects are spatial peak values in the entire body while the values for sensory effects are spatial peak values in the head of the exposed subject. Both the ALs values and ELVs used in the directive are based on the recommended values of the International Commission on Non-Ionizing Radiation Protection (ICNIRP).

Table 1: EU directive health and sensory effects ELVs for induced internal electric fields, and low and high ALs values, for 50 Hz external electric fields. The RMS values are derived from the peak values.

	Health effects ELVs (mV/m)	Sensory effects ELVs (mV/m)	Low ALs (kV/m)	High ALs (kV/m)
Peak value	1100	140		
RMS value	778	99	10	20

If the ALs are exceeded, the employer must demonstrate that the health effect and sensory ELVs are not exceeded or take all necessary precautions to limit the exposure to an allowed level. Thus, even if the ALs values are exceeded it does not necessarily mean that the working conditions are deemed unsafe, instead the ELVs are the determining factor. In a situation where the ALs are exceeded, the employer is obliged to carry out measurements or calculations that prove that the ELVs are not surpassed. The assessment needs to take into account uncertainties in the process, such as numerical errors, variations in human model phantoms as well as in tissue and material electrical properties.

In addition to the safety limits introduced previously, the directive also states that workers need to be properly informed and educated of the risks of electromagnetic field exposure. Special attention is to be taken when workers from a particular risk group, such as people with medical devices or pregnant women, are concerned. Also appropriate health surveillance has to be carried out.

ICNIRP Guidelines

The basis for the restrictions given in the EU directive is derived from the recommendations made by ICNIRP, in their “Guidelines for limiting exposure to time-varying electric and magnetic fields (1 Hz to 100 kHz)” document [3]. The document describes the health effects of electromagnetic fields, gives guidelines for limiting EMF exposure, gives rationale for these restrictions and gives some ideas for protective measures.

The health effects of EMF have been studied thoroughly over the years, by individual scientists and scientific panels. Attention has been paid to neurobehavioural effects, effects on the endocrine system and on reproduction and development. The effects of EMF on the development of cancers, neurodegenerative and cardiovascular disorders has also been studied. According to research that has been conducted so far, the only verifiable although temporary health effects of EMF exposure are direct stimulation of nerve and muscle tissue in strong external fields. This stimulus can cause perceived annoyance, pain or other effects on the nervous system. Such effects are for example, retinal phosphenes, that is a visual perception of dim flickering lights in the peripheral vision, and in some cases short term disruptions in brain visual processing and motor coordination. These neurobehavioural effects are the main bases for the recommended occupational and public exposure limits.

The basic restrictions by ICNIRP have been set so that there is no chance of retinal phosphenes occurring. This measure should protect from all effects on brain function. In some occupational cases some transient effects e.g. retinal phosphenes are acceptable, as these do not cause long-term or pathological effects. In work duties where transient effects occur, the personnel should have prior knowledge about these effects and be willing to experience them. The basic restrictions have also been set with peripheral and central nerve stimulation in mind. The limits are set so that no stimulation occurs. The chance for even the smallest stimulus is eliminated because the gap between perception and pain is relatively small.

Strong EMF also have indirect effects in the form of contact currents and spark discharge. These occurrences can cause pain when the potential difference is large between the subject and a touched object. These surface electric-charge effects are also taken into account within the recommended restrictions.

No long term health effects of EMF have been conclusively proven although EMF exposure has been categorized as “possibly carcinogenic to humans”, due to some epidemiologic results on childhood leukemia [4]. Still, no direct causal relationship with exposure and the leukemia have been proven and as such these results are not used as a basis for the exposure guidelines.

Previous Studies by Fingrid

Since the first 2004 EU directive came out, Fingrid has taken action to ensure that the working conditions remain safe, at all times, at its power substations and power lines. Normally, all substations in Finland are unattended by personnel and are instead controlled and monitored remotely. The facilities and power lines are only visited on inspection visits or during maintenance, modification or construction work [5]. To ensure the safety of workers and compliance with the EU directive in these instances, Fingrid has conducted various EMF measurements at its facilities as well as follow-up research on the topic of EMF exposure.

Electric and magnetic field strengths have been measured at multiple different 110 kV, 220 kV and 400 kV substations by Korpinen, et al. [5–9]. Some measurements concentrated on mapping the electric field strengths in larger areas within the substations, while other measurements were conducted at specific locations to simulate varying work tasks performed next to certain equipment. Fingrid has had a practice of measuring the electric and magnetic fields by attaching a probe to a wooden tripod via dielectric material to keep the influence of the tripod itself to a minimum to the measurements. The field magnitudes have usually been measured at 1 m height or around head level (1.7 – 1.8 m). The key results of the field strength measurements are that ALs values are only exceeded at 400 kV substations and even at these facilities locally. Maximum field values most often occur under crossing cophasal main and bay busbars. In these situations, both conductors have the same potential and phase angle and therefore a higher total field ensues. High electric field values also occurred under two parallel busbars with the same potential and phase angle.

In addition to the assessments of field strength, Fingrid has also conducted current density and contact current measurements for typical work tasks using a helmet-mask measurement system in collaboration with Korpinen et al. [6, 10, 11]. The results from these helmet experiments could be directly compared with the old 2004 EU directive which declared the action levels and exposure limit values in contact currents (mA) and current densities in the body (mA/m^2) respectively. According to the measurements performed, the ELVs are not exceeded in any investigated work task or at any location be it a 400 kV substation or power line. The same measurement system is used in measurements conducted for this thesis. The helmet-mask measurement system will be described in detail in the methods section of this work. Additionally, the system will be vetted against the computational simulations.

As previously mentioned, the current density and contact current values could be previously directly compared with the 2004 EU directive safety values. With the new 2013 directive, this is no longer possible. The basis for the new safety limits, the internal electrical fields induced to a human body, cannot be directly measured. Instead, numerical analysis and methods are required. For these reasons, Fingrid has previously collaborated with Tarao et al. to perform human model dosimetry studies. The studies have concentrated on finding a link between contact current and internal electric fields [12]. Finding a clear relationship between these two would make it possible to reliably transform the experimental contact current data to represent the internal electric fields, and compare these values to the safety values presented in the

new directive. According to the studies, there is a strong interrelationship between the neck currents, measurable with the helmet-mask measurement equipment, and the induced electric fields in the nervous system tissues. Relationship between the induced electric field and the external field strength is also demonstrated [13]. Estimation of induced fields directly from the external field strength is reported to be more difficult as the geometry of the surrounding environment has a large effect on the external field uniformity and thus on the induced fields. Nevertheless, the 2016 study by Tarao et al. presents an estimation method for the induced fields, but the method only works in fairly limited cases [14].

Other Studies

After studies concluded by Fingrid in collaboration with others have been addressed, the next steps is to take a general look at other studies handling dosimetry of ELF electric fields. Generally speaking it can be said that dosimetry of ELF electric fields has not been in the focus of the scientific community. Traditionally the majority of dosimetry studies have concerned ionizing radiation and magnetic fields, especially in the context of medical treatments and medical devices. Another major interest of research has been radio frequencies, especially specific energy absorption rate (SAR) studies, which have been conducted to ensure the safety e.g. of cell phones and other wireless devices.

One of the most important contributors in the field of ELF electric field dosimetry is Peter Dimbylow. Dimbylow worked at the British Health Protection Agency, formerly the National Radiological Protection Board and began his work on electromagnetic field dosimetry in the mid 1990s. The work began by constructing a high resolution human voxel based phantom model NORMAN [15]. During the late 90s, Dimbylow conducted multiple dosimetry studies on the newly made phantom. These studies included 1 MHz–1 GHz SAR and 50 Hz–10 MHz magnetic field exposure scenarios [15, 16].

Finally, in the year 2000 Dimbylow published his first article on electric field dosimetry utilizing the newly developed high resolution phantom model [17]. In this paper vertical, homogeneous, 1 kV, 50 Hz–10 MHz electric field exposure was studied using a finite-difference time-domain method and the NORMAN phantom model. Both isolated and grounded scenarios were considered. The results of this study were reported according to the standards of the time, in induced internal current densities and the values averaged over an area of 1 cm^2 [18]. Thus, the results are not directly comparable with newer studies, such as this thesis. The main findings of the study were that the current densities depend on the cross section area of the body. Hereby, the strongest current densities occurred in the neck, knees and ankles. Dimbylow also calculated how strong the external electric fields would have to be to cause the ICNIRP guideline safety limits for induced current densities to be exceeded. According to the article, a 50 Hz electric field would have to be 47.8 kV/m strong to cause current densities exceeding the guideline limits. When this field strength is compared with the external 10 kV/m field strength safety limit proposed by ICNIRP, it can be concluded that the ICNIRP and the EU directive safety values are fairly conservative.

Dimbylow continued on his work through the 2000s, developing a new female phantom model NAOMI, as well as a pregnant phantom model [19, 20]. Also an articulable model of the NORMAN was developed [21]. For these new models simulations similar to the previous electromagnetic studies were performed. Additionally, more focus was put towards the analysis of ELF electric fields than before. For example, the orientation of the incident electric field was varied. In addition to a vertical electric field, also horizontal, side to side and front to back fields were studied. After the basic research on ELF electric fields was concluded, Dimbylow shifted his attention on the effects of phantom posture and the difference in results

between different phantom models [22]. In the cross-phantom comparisons a total of six adult models, eight child models and seven pregnant models were compared. These new studies also reported the results as induced internal electric field strengths, in addition to current density values. Unfortunately, the results are still averaged over 1 cm^2 instead of the $2 \times 2 \times 2 \text{ mm}^3$ cubes used in this thesis and recommended in the current EU guidelines [23]. Hereby, the results are not fully comparable with the 2010 EU directive or this work. The key findings of these studies are that the orientation of the external electric field, the posture of the phantom as well as the phantom model chosen all affect the induced currents and electric field strengths in a considerable degree. Another important observation that can be made is that, the ICNIRP safety limits are rather conservative. External field strengths far stronger than the ones expressed in the guidelines are needed to produce induced currents exceeding safety limits.

The vast majority of all studies performed on ELF electric fields concern homogeneous fields and cases where the human body is grounded through its feet. In reality most exposure scenarios occur in nonuniform fields and the body is isolated from its surroundings or grounding occurs through the hands. Thus, it can be said that dosimetry studies concentrated on ELF electric fields have usually been fairly narrow. In most cases, studies have only addressed phantoms standing in uniform fields without any geometry around them. The few studies that have focused on inhomogeneous fields have only included a very limited amount of geometry. Additionally, the geometry modelled has been fairly rough. In this sense, the work concluded in this thesis is one of the first of its kind: Time dependent heterogeneous electric fields produced by realistic geometry, simulated at high accuracy.

3 Methods

This chapter discusses the methods used throughout this thesis work. The chapter is divided into subsections presenting the methods separately for experimental measurements and for simulations. The experimental methods section concentrates on describing measurements concluded at a Fingrid electrical substation, while the simulation section strives to explain how the simulation code works and what assets are utilized in the simulations.

Measurements



Figure 1: Overview of the studied area. Objects of interest numbered: 1. Circuit breaker 2. Service platform 3. Current transformer.

This chapter copes with the experimental electric field strength measurements conducted at a Fingrid electrical substation. The measurement location, the measurements conducted, measurement methods as well as the equipment used will be presented and discussed in detail.

The measurements were conducted on the 28th of June 2017. The weather was fair, with mild wind and a temperature of little under 20°C. That is favourable weather for electric field measurements, where air humidity can have a considerable effect on the measurement results. The measurement location was a typical, modern, Finnish 50 Hz electrical substation. The substation in question has both 110 kV and 400 kV sections, with voltage conversion between the two sides. Our measurements took place in the near proximity of circuit breakers on the 400 kV side. More accurately next to two adjacent breakers operating at the same voltage and phase. This specific location within the station was chosen because, as earlier research indicates, the maximum electric field strengths occur at locations similar to this. An overview picture of the studied area is shown in figure 1. All work done at the substations

was performed under the supervision of professionals to stay safe.

The goal of the experimental measurements was to produce data that can be later directly compared with simulated results. The comparison is made to validate that our simulations produce results that are consistent with the real world. Further on, once the simulations are proven to be reliable, deductions of working safety can be made. The simulation environment is modelled directly after the measurement site to keep the results analogous. The modelling of the locale as well as the simulated results will be presented in later chapters.

During the measurement day, a total of five different measurements were carried out: A mapping of field strengths around one of the circuit breakers; a field strength measurement at the circuit breaker service platform; a field strength measurement underneath the cophasal busbars; a measurement of the influence of an adjacent human body on the external field; and lastly induced currents measurement in the vicinity of the circuit breaker using the helmet-mask measuring apparatus. All electric field strengths were measured using a Narda NBM-550 broadband field meter and a Narda EHP-50F electric and magnetic ELF field probe. Both apparatuses are pictured in figure 2 below. The meter and probe were connected via a relatively long optical cable. The meter and the probe are kept apart from each other, to keep the influence of the measurer's body on the measured external field to the minimum. The distance between the probe and the measurer was kept at over five meters at all times to eliminate any negative effects. The probe itself was attached to a wooden adjustable tripod, for easy height adjustment. The stand has to be of a non-conductive material to keep the external field intact from any disruptions caused by conductive objects.



Figure 2: The Narda NBM-550 broadband field meter in the front, and the Narda EHP-50F electric and magnetic ELF field probe in the back.

The general mapping of electric field strengths around the circuit breaker was conducted by marking down a five by nine meter grid with one meter spacings. The field strengths were measured at each grid point at an 1.7 m height from the

ground. This measurement procedure resulted in 41 distinct field strength values being measured. Additionally, a single measurement was taken from a greater height of three meters, to see how the distance from the ground level affects the field strengths.

The electric field strengths at the circuit breaker service platform, location shown in figure 1, were measured at three different heights relative to the platform and at two different distances from the control unit cabin. The three heights were 1.16, 1.5 and 1.7 meters, and the distances from the cabin door 0.2 and 0.65 meters. The measurements were taken at different heights to get insight on how much the surrounding conductive objects, such as the cabin and railings of the platform, shield a working person from the external fields. The same reasoning stands for changing the distance of the measurement point from the cabin door. Additionally, a measurement with the control cabin door open was taken. This was done to observe how the open door would influence the surrounding field strengths.

The influence of the human body on the surrounding electric field was also measured. This was achieved by keeping the probe stationary at the height of 1.7 meters, while our 1.9 m tall subject got progressively closer to the probe by taking twenty to ten centimeter steps. The distance from the subject to the probe was measured from the middle point of the tripod to the tip of the shoes of the subject. The measurements began from a distance of 1.8 meters and concluded when the subjects toes were exactly underneath the probe. The aim of this measurement was to get quantitative data on the distortion of the external electric field caused by a human body. The data acquired is used to validate that the effect of the body on the EMFs is modelled correctly in our simulations.

Lastly, currents induced to the body by the electric fields were measured using the helmet-mask measurement system. The measurement apparatus being worn by our 1.7 m tall test subject is pictured in figure 3 below. The induced currents were measured at multiple locations near the 400kV circuit breaker: on the service road in front of the breaker; on the service platform with the control cabin door closed and open; next to the service platform; and lastly underneath the cophasal busbars.



Figure 3: The helmet-mask measurement system being worn.

Helmet-Mask Measurement System

The measurement equipment, pictured in figure 4, consists of a protective helmet that has been coated with a conductive copper layer; a conductive metal mask; a medical electrode; and two current meters. When the system is in use, the helmet and mask are worn and the electrode is attached on the forearm of the test subject. When the helmet is worn, it covers the whole head of the test subject. Hereby, all current normally induced into the head is induced to the helmet instead. This induced helmet current can be measured using a current meter attached between the helmet and the ground potential. The total current induced to the body is also measured. This is done by attaching a second current meter in series with the first one and connecting also the arm electrode to the grounding wire. All currents induced to the torso and limbs of the subject flow through the electrode and the second current meter into the ground.

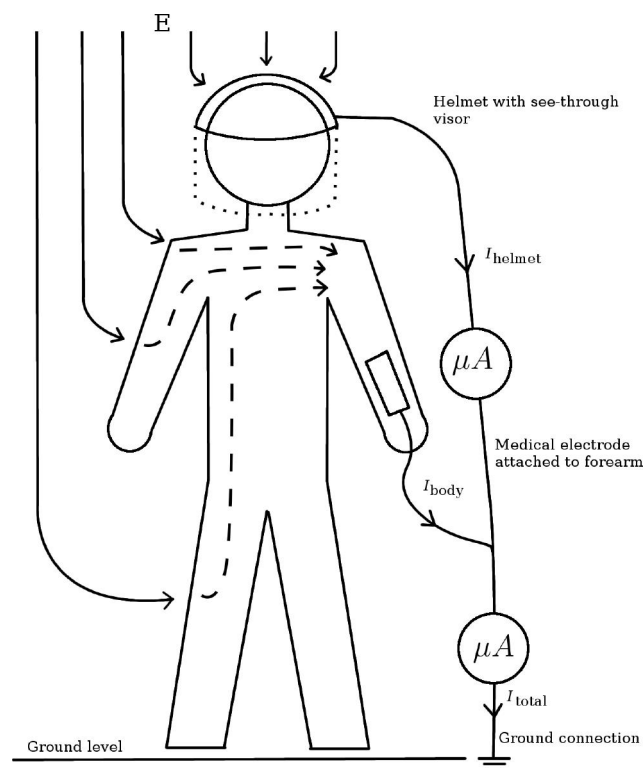


Figure 4: Working principle of the helmet-mask measurement system.

In a simplified working scenario, the worker is standing in a roughly vertical electric field and is isolated from the ground potential by shoes and other clothing. In a case like this, the induced currents flow from the top of the body towards the feet and vice versa depending of the phase of the surrounding electric field. The flow of currents through the body bring about areas with different current densities. These current densities depend on the current magnitude, tissue conductivities and the cross-section area the current is flowing through. From these premises, the goal is to solve the induced electric field strengths in the CNS and in the whole body.

Calculating the exact field strengths from two current measurements is not possible, thus resorting to approximations is necessary. A study by Korpinen et al. has determined that the internal electric fields in the head and CNS can be approximated from the current density in the neck of a subject [6]. This is a somewhat reasonable assumption as all currents induced to the head flow through the relatively narrow neck, producing an area of high current density. The head's maximum current density can be assumed to be located in this area.

Calculating the current density in the neck from the measured helmet current is simple. Calculating internal electric field strengths from current densities is also possible. Thus an equation for the induced electric field strength can be formulated using the measured helmet-current. The current density can be calculated using equation (1), where A is the cross-section area of the neck. This area can be calculated by assuming that the cross-section is a circle and using the circumference of the neck. In our calculations the neck circumference $p = 35$ cm. Further on, the internal electric field can be calculated from the current density using formula (2). The conductivity is assumed to be the average conductivity of the human body $\sigma \approx 0.1$ S/m. Additionally a scaling factor, constant $c = 0.82$, is used to scale the electric field strength to better account for the geometry at a typical measurement location. The scaling factor has been chosen by Korpinen et al. in accordance with their studies concluded in collaboration with Fingrid Oyj. [6]

$$J = \frac{I}{A} = \frac{I \times 4\pi}{p^2} \quad (1)$$

$$E = \frac{c \times J}{\sigma}, \quad c = 0.82 \quad (2)$$

Using the previously introduced approximation to calculate induced current densities in the head and CNS has been reported to produce sensible results [13]. One goal for this thesis is to confirm these findings using computational simulations. We are also interested in how well the equation can estimate internal field strengths in other parts of the human body.

Modeling the Environment

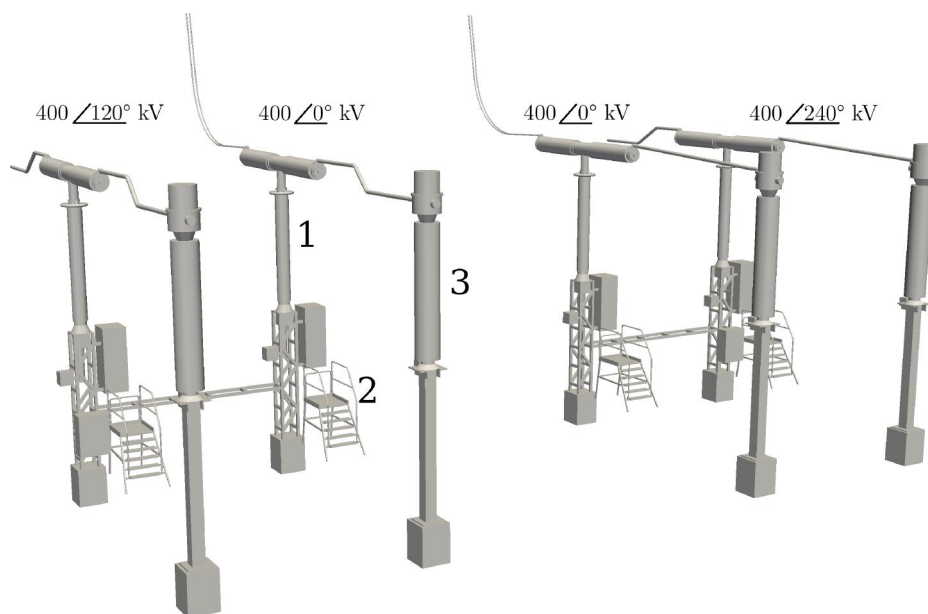


Figure 5: Modeled geometry with four circuit breakers (1), service platforms (2) and current transformers (3). The operating voltages and phases are also shown.

This chapter presents the 3D models created for the computational field simulations and covers how the 3D models were made as well as what software was utilized. The chapter also discusses design choices made during the modelling process and explains the reasoning behind these choices.

An accurate 3D model of the environment is an essential part of the computational simulations. It is important that the scales and distances between objects are true to life so that comparability of simulated and experimentally measured results is preserved. Smaller details of the 3D model are also important for accurate simulation results. Details such as the roundness or sharpness of corners and edges of the modelled objects as well as the exact locations of these features have a significant effect on the electric field flux surrounding the geometry. The roundness and sharpness of object features are especially important, because high electric field strengths tend to concentrate on pointed edges of conductors. This occurs due to free electrons accumulating at locations where the object curvature is the sharpest. Rounded or flat surfaces on the other hand have a more even distribution of electrons and thus, more even electric fields surrounding them.

As previously stated, the main interest of this study is the electric fields at the 400 kV circuit breaker and its immediate surroundings. Thus, the bare minimum objects to be modelled for the simulation environment are the circuit breaker itself, the busbars connected to the breaker, as well as the service platform and the stairs in front of the breaker. The follow up question is: How much of the surrounding geometry should be added to the simulation space? From the previous studies done by Fingrid, it is known that the strongest electric field strengths do not occur directly

underneath the circuit breakers, but between two circuit breakers operating at the same voltage and phase. Hence, it is obvious that at least two adjacent circuit breakers should be included in the simulation environment for accuracy. Additionally, a fourth circuit breaker further to the right is included to keep the scene symmetrical. These four neighbouring breakers occupy an area of roughly twenty meters wide. From this spacing, it is reasonable to assume that also other live or grounded objects within a radius of ten meters may have a significant effect on the external electric field. Thus, also current transformers in front of the circuit breakers are modelled into the scene.

The actual 3D modelling of the objects was done with FreeCAD, an open source parametric 3D computer-aided design (CAD) program. The choice to use this particular piece of software for modelling, instead of a commercial alternative, was due to its Linux support. For the sake of simplicity, the majority of models were created by combining simple geometric shapes such as rectangular cuboids, cones and cylinders together. Few parts, such as the busbars and power lines with bends in them required more elaborate shapes. For these splines and bodies of revolutions were utilized. For all modelled objects, 2D CAD blueprints with measures were used as references. The blueprints were provided by Fingrid and contained both overview pictures of the substation as well as more detailed illustrations of individual components. As additional reference points, measurements and photos taken while visiting the electric substation were used.

Once the separate models were finished, the objects were positioned in correct locations relative to each other and the ground level. The files were converted into Visualization Toolkit (.vtk) file format and imported to MATLAB for simulations. The outcome of the modelling work done is presented in figure 5.

Altogether, the models are true to life in dimensions but are slightly lacking at the detail level. One example of the absence of finer detail is structural metal beams used in the stairs, for instance. Most of the real structures are assembled out of L-profiled steel beams, but in the models these are substituted with solid rectangular beams. However, these small differences in details are of no concern as the final simulation results are not affected. This is due to the simulation grid utilizing $4 \times 4 \times 4 \text{ cm}^3$ cells which conceal the smallest object details. The three most important aspects of model details, regarding to simulation accuracy, are correct model dimensions, the correct positioning of objects relative to each other, and accurate representation of sharp edges and smooth surfaces where they are needed. All of these three conditions are realized well in the models created.

Human Phantom Model

Computational human phantoms are models of the human body used in computational analyses. Phantom models have been used since 1960s in various radiation dosimetry studies both involving ionizing and non-ionizing radiation. Since the 1960s, over 140 different computational human phantoms have been reported in literature. Generally, these phantoms can be categorized into three generations: First, stylized phantoms which depict the human body and its organs using mathematical equations of geometrical shapes, such as ellipsoids, cones and spheres; Secondly, voxel based phantoms where imaging data from magnetic resonance imaging images, computed tomography scans or photos of anatomical slices is segmented into a 3D representation of the human body using voxels; and lastly boundary representation phantoms which present the body and its various organs using polygonal meshes. The different types of computational phantoms have their own advantages and weaknesses. The stylized phantoms are simplified representations and thus simulations are fast to run but lacking in detail. Voxel based phantoms can be accurate down to sub millimeter scales, but are static representations of the body and as such have difficulty in representing different postures or movement caused by breathing or other vital functions within the body. Lastly, the polygon mesh based phantoms are easily spatially transformed, can be postured using real motion tracking data and it is even possible to model time dependent bodily functions such as breathing. [24]

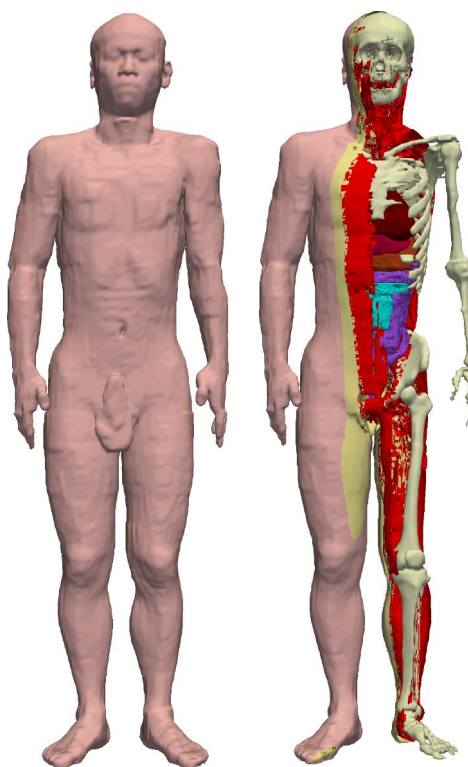


Figure 6: Taro human phantom model. Bone, fat, muscle and skin tissues visible, as well as the hearth, liver, stomach and intestine.

For our study, an accurate representation of a real human body and high resolution

was of most importance. Hence, a voxel based phantom was a natural choice. The majority of simulations were run using the realistic high-resolution whole-body voxel model of a Japanese adult male, Taro developed by Nagaoka et al [25]. The Taro model is pictured in figure 6. The Taro phantom model is 172 cm tall and weighs 65 kg. The phantom has been segmented into $2 \times 2 \times 2$ mm³ cubes and each cube has been assigned a tissue type. The taro model has a total of 51 different tissues. Some of the tissues are slightly over represented in the model compared with a real human. For example, there is more skin mass wise in the phantom than in a real human body. This is due to voxelization of the body. Thin or small volume tissues appear thicker due to the minimum detail size of 2 mm.

In the case of simulating exposure to extra low frequency electromagnetic radiation, the conductivities of different tissue types are important. Our conductivity values are calculated from a parametric model developed by Gabriel et al. and slightly modified by Dimbylow to better account for low frequencies [26]. This particular conductivity model was specifically chosen because it has been widely used in the literature. All tissue types in the Taro model and their conductivities are listed in table 2. The parametric model has been formulated from experimental measurements conducted with 10 Hz – 20 GHz fields on animal tissue, human autopsy materials as well as some in vivo human measurements [27]. For example, the conductivities of the tongue and skin have been measured from a living test subject. It is noteworthy to notice that the measured dielectric properties of tissues are not exact. There can be considerable differences in conductivity values between individuals. In fact, Gabriel et al. noticed that the variation between individuals can be greater than the variation between species. This also explains why it is acceptable to use values derived from animal measurements. Another factor to take into account is that the dielectric properties of tissue may vary depending of orientation. For example, the longitudinal and transversal properties of muscle tissue differ significantly. Hereby, some simulation error arises from the uncertainties in the conductivity values.

In addition to the Taro phantom also, four other phantom models were utilized for validation purposes and to study how the phantom size and shape affects induce internal fields. These four phantoms are: Hanako, the female version of the Japanese realistic whole-body voxel model [25]; Duke and Ella, the adult male and female phantoms from the virtual family project [28]; and NORMAN, the phantom model developed by Dimbylow during his work in the British Health Protection Agency [15].

Table 2: Segmented tissues in Taro phantom and the corresponding tissue conductivities.

Tissue / bodily matter	Conductivity
Adrenal gland	0.35
Air (Internal)	0
Bile	1.4
Bladder	0.21
Blood	0.7
Bone Marrow and Cancellous Bone	0.07
Cartilage	0.18
Cavernous Body	0.35
Cerebellum	0.1
Cerebro spinal fluid	2
Cornea	0.5
Cortical Bone	0.02
Diaphragm	0.35
Duodenum	1.09
Esophagus	0.52
Eye lens	0.26
Eye sclera	1.5
Fat	0.04
Gallbladder	0.9
Gray Matter	0.1
Heart	0.08
Hypothalamus	0.1
Kidney	0.09
Large Intestine	1.2
Large Intestine Contents	0.35
Ligament	0.27
Liver	0.07
Lung	0.2
Muscle	0.35
Pancreas	0.35
Pineal Glands	0.1
Pituitary	0.1
Prostate	0.42
Salivary gland	0.35
Seminal Vesicle	0.35
Skin	0.1
Small Intestine	1.09
Small Intestine Contents	0.35
Spinal cord	0.03
Spleen	0.09
Stomach	0.52
Stomach Contents	0.35
Tendon	0.27
Testis	0.35
Thalamus	0.1
Thyroid	0.52
Tongue	0.3
Tooth	0.02
Trachea	0.3
Urine	0.7
White Matter	0.06

The Simulation Algorithm

This chapter presents the simulation algorithm used to run the simulations. The simulation code utilized in this thesis is based on software created by Laakso and Hirata for the purpose of computational modelling of induced electric fields during transcranial magnetic stimulation [29]. The majority of the simulation code is implemented in MATLAB, with an exception of a few computationally most demanding functions that are written in C and are run outside MATLAB as MEX functions. This is done to decrease simulation run times and to save system resources. In addition to the simulation code, this chapter also tries to explain some of the physics behind the electric field calculations.

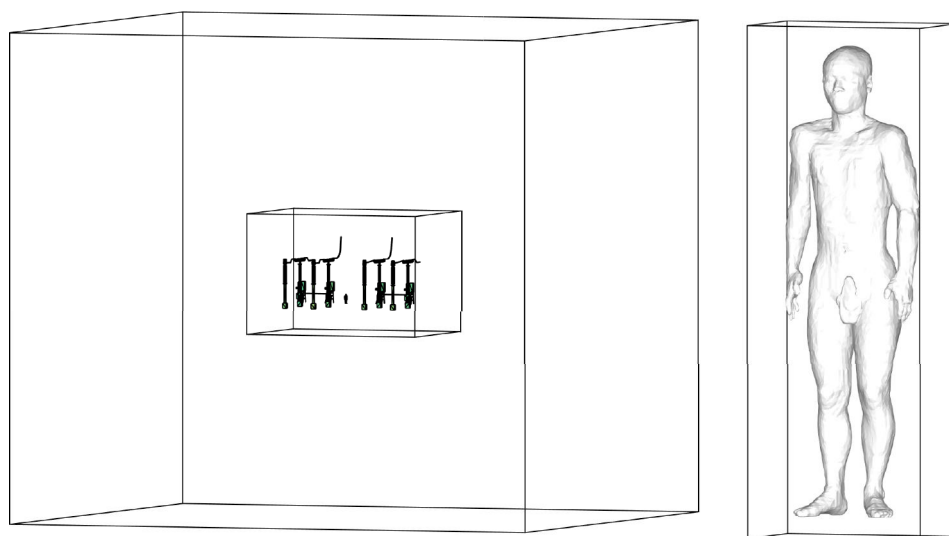


Figure 7: The three domains used in the simulation. The two larger ones enclose the geometry and the smallest one the phantom.

The simulation begins with loading all the modelled geometry to MATLAB's memory and positioning the user chosen human phantom model to its desired location. All the objects are defined either as electric sources, with electrical potentials attached to them, ungrounded conductors, or as insulators with material dependent electrical permittivities. Following the geometry setup a total of three different sized simulation domains are created. The domains are presented in figure 7 together with the geometry and the phantom model for scale comparison. The domains are in principle volumes within which all the electric field calculations are performed. The domains are created according to the geometry itself and variables defined by the user. The domains contain data arrays of the permittivities of the individual voxels forming the simulation volume. The user definable variables are "padding", the amount of empty space encasing the geometry, and "grid size", the size of the voxels the simulation volume will be divided into. A total of three different domains are used in the simulations, each differing in volume and grid size. The simulation gradually advances into using a smaller simulation volume and grid size. This is done to solve

the external electric field surrounding the studied phantom model at an ever more accurate level. Each simulation domain has a boundary condition attached to it. This condition defines the electric potential on the outer surface of the domain. When switching between domains, the boundary condition is derived from the previously used larger domain. The principal reason for using multiple domains is to regulate the usage of system resources during the simulations as well as optimizing the simulation run times. The external electric fields are only simulated at the most accurate 2 mm scale in the near proximity of the human phantom model. Elsewhere, larger grid size and thus, less accurate electric field strength values are adequate.

All electric field simulations are performed twice at two different phases of alternating current (AC). This is done so that the time dependent fluctuations of the electric fields in an AC system are taken into account. The phase difference between the two studied time points is 90°. A simplified flow chart of the simulation code is shown below in Simulation algorithm below.

Simulation algorithm

- 1 : Load geometry into MATLAB's memory
 - 2 : Load phantom model and position it

 - 3 : **repeat** twice with 90° phase difference
 - 4 : Define geometry objects as electric sources, conductors or insulators
 - 5 : Set electric potentials for grounded and energized objects
 - 6 : Create simulation domain
 - 7 : Create a box bounding the geometry and add empty padding
 - 8 : Create a 3D array and store geometry permittivity data
 - 9 : Solve scalar potentials inside the domain using FEM
 - 10 : Calculate electric potentials of ungrounded and non-energized conductors
 - 11 : Resolve the scalar potentials using updated geometry using FEM
 - 12 : **end**

 - 13 : Define boundary conditions for smaller domain from previously solved domain

 - 14 : **repeat** twice with 90° phase difference
 - 15 : Steps 3-9 and 13 for middle domain
 - 16 : **end**

 - 17 : **repeat** twice with 90° phase difference
 - 18 : Steps 3-9 for innermost domain
 - 19 : **end**

 - 20 : **repeat** twice using the solved external fields with 90° phase difference
 - 21 : Create surface electric sources for the phantom from the solved external field
 - 22 : Solve phantom internal scalar potentials using FEM
 - 23 : **end**

 - 24 : Sum solved electric fields differing in phase using superposition principle
-
-

The properties of the domains used in the simulation have significant effects on the simulation end results. For this reason, the properties of the used domains will be explained in detail in the subsequent paragraphs: The outermost and largest domain spans over the whole geometry and includes a considerable amount of empty space around the geometry. As a matter of fact, the geometry spanning a volume of $16 \times 24 \times 13 \text{ m}^3$ is padded by a forty meter empty border region. The grid size utilized in the outermost domain is $9 \times 9 \times 9 \text{ cm}^3$. The reason for including such a large amount of empty space around the actual modelled geometry is that the outer surface of the domain has a boundary condition defining that the electric flux cannot pass the boundary and is instead confined within the domain. This results in a situation where the electric flux ends up circling around the geometry at the outer layers of the domain. A boundary that confines the flux like this is naturally unrealistic and causes errors in the calculated electric field strengths. Fortunately, these adverse effects of the used boundary layer type can be circumvented by padding the geometry with plenty of empty space as done here, giving plenty of room for the electric flux to freely circulate in the outer regions of the domain without affecting the field within the area of interest. An alternative and possibly better solution to using empty padding would have been to develop a boundary layer that has absorbing properties. Unfortunately creating a solution like this was not possible in the time frame of this thesis work. Nevertheless, we might speculate that if such absorbing boundary layer was created, the accuracy of the final results of the simulations would not be affected much, but as a benefit the run times of the simulations would have been quicker because of the simulated volume being significantly smaller.

The second domain also contains the whole geometry within it, but has less empty padding around it. The amount of padding used is five meters in each direction and a voxel size of 4 cm is utilized. The boundary condition for this inner domain is derived from the intersection of the two nested domains. In practice the boundary condition is set so that the potential at the boundary layer is fixed to match those occupying the same locations in the larger domain. The potential values are interpolated from the larger grid size to the new smaller one to warrant a smoother transition between grid sizes. Having this boundary condition defined eliminates the need of an empty region for the “circulating” electric flux in the inner domains. This second simulation detail level is used to solve the external electric field strengths for the whole geometry. Hereby, the external electric fields are simulated at 4 cm voxel resolution for the whole geometry.

The final and smallest domain surrounds only the human phantom. This domain has a minuscule amount of padding, 1.6 cm and uses a voxel size of 2 mm. The boundary condition is defined the same way as previously. This smallest domain serves the purpose of solving the external electric field at the same resolution as the phantom is modelled at. When the resolutions match, the external field is easily and accurately converted into current sources. These current sources are positioned on the surface of the phantom for the calculation of the internal electric fields.

The phantom internal electric fields are solved using the same solver utilized in the external field calculations. The only difference being that all tissues within the phantom have distinctive conductivities, compared with the three options on the

external calculations: conductor, insulator or air.

Now that an overview of the simulation algorithm has been established, a closer look at the solver used to solve the external and internal electric fields is taken. The solver solves the electric scalar potential for each voxel in the simulation domain from the elliptic partial differential equation, equation number (17). The problem is discretized before it is fed to the solver using finite element method (FEM), specifically the Galerkin method [29].

The elliptic partial differential equation for the scalar potential can be derived from Maxwell's equations (3) - (6) in the case of the external electric field,

$$\nabla \cdot \mathbf{D} = \rho \quad (3)$$

$$\nabla \cdot \mathbf{B} = 0 \quad (4)$$

$$\nabla \times \mathbf{E} = -\frac{\partial \mathbf{B}}{\partial t} \quad (5)$$

$$\nabla \times \mathbf{H} = \frac{\partial \mathbf{D}}{\partial t} + \mathbf{J} \quad (6)$$

and from equations (7) & (8) defining the relation between the electric displacement field \mathbf{D} and the electric field strength \mathbf{E} , as well as the relation between the current density \mathbf{J} and the field strength.

$$\mathbf{D} = \varepsilon \mathbf{E} \quad (7)$$

$$\mathbf{J} = \sigma \mathbf{E} \quad (8)$$

In the case of the external electric field, the medium is air or an insulator and thus the permittivity can be thought to be the same as the permittivity of vacuum $\varepsilon = \varepsilon_0$. The conductivity of air $\sigma = 0$. Now if we take the divergence of both sides of equation (6) we get

$$\nabla \cdot \left(\frac{\partial \mathbf{D}}{\partial t} + \mathbf{J} \right) = 0 \quad (9)$$

due to the divergence of a curl always being zero. In this case, $\mathbf{J} = 0$

$$\nabla \cdot \frac{\partial \mathbf{D}}{\partial t} = 0, \quad (10)$$

which leads to the divergence of electric displacement field also being zero:

$$\nabla \cdot \mathbf{D} = 0. \quad (11)$$

Now if equation (7) is combined with the result of equation (11) we arrive at

$$\nabla \cdot \varepsilon \mathbf{E} = 0 \quad (12)$$

To advance further a simple approximation regarding the electric fields has to be made. The electric fields at the electric substation are of extreme low frequency (50 Hz). Therefore, it is reasonable to think that the electric field and hereby the magnetic flux generated by the energized wires barely changes at all at any given point of time. This can be formulated as below

$$\frac{\partial \mathbf{B}}{\partial t} \approx 0 \quad (13)$$

The approximation is called the quasistatic approximation and it holds true to any electric field with a frequency lower than 1 MHz.

Now the Faraday's law of induction, equation (5), takes the form

$$\nabla \times \mathbf{E} = 0 \quad (14)$$

which implies that the electric field can be expressed as the gradient of the scalar potential:

$$\mathbf{E} = -\nabla\phi \quad (15)$$

When the result of the quasistatic approximation is combined with equation (12) where we last left off, we arrive at

$$-\nabla \cdot \varepsilon_0 \nabla \phi = 0 \quad (16)$$

This result can be generalized to the final equation used in solving the scalar potential both in the case of the external field as well as the phantom internal field:

$$\nabla \cdot \varepsilon \nabla \phi = 0 \quad (17)$$

where ε is chosen according the use scenario.

The simulation algorithm returns the final electric field strengths in volts per meter V/m. This unit of field strength \mathbf{E} can easily be converted into current density \mathbf{J} , using formula (8). This is a useful property, as it enables us to solve the currents flowing through the phantom and thus, direct comparison with currents measured with the helmet-mask measurement system.

In addition to the scalar potential formula, there is another significant result that can be derived from the above formulas as a side result. Namely a condition that states how the external electric field can be transferred into the phantom for internal field strength calculations. This condition is presented in equation (18). In principle the condition states that the charge density on the surface of the phantom can be depicted using current sources. These current sources can be used further to simulate the internal electric field. The equation can be derived by combining equations (9) and (3) as shown below.

$$\nabla \cdot \mathbf{J} = -\frac{\partial}{\partial t} \nabla \cdot \mathbf{D} = -\frac{\partial}{\partial t} \rho \quad (18)$$

In practice this conversion is performed by calculating the electric flux entering each voxel on the surface of the phantom. From the flux, the charge of each voxel is

easily calculated. The charge of a voxel is further converted into an electric current source. The most difficult task in this process is to accurately calculate the amount of flux entering a voxel on the surface of the phantom. The largest issue is that the external electric field is extremely distorted close to the phantom. The distorted region is two voxels wide and is caused by the staircase approximation of the phantom model. In our implementation, the problem is circumvented by approximating the flux entering a surface voxel from the data of three successive voxels at a distance from the surface. The data of the two very closest voxels are ignored and the calculations are done using three consecutive voxels, two voxels away from the surface. In our approximation it is assumed that the flux density weakens in the second power of distance from the phantom surface. Thus, by fitting a second order polynomial to the data of flux flowing through the three voxels at distance from the surface, an approximation of the flux entering the voxel on the surface is obtained. This approximation turns out to be a reliable one, as will be later demonstrated in the next chapter concerning validation of methods.

4 Validation of Methods

This chapter covers how it was made sure that our simulation algorithm produces reliable results. Two distinctive validation processes were utilized: Firstly, a set of simplified simulation scenarios were run that could also be solved analytically. The results of the two solution methods were compared against each other and a relative error percentage was calculated for the numerical solution. Secondly, a number of more complex simulations similar to ones previously reported in the literature were run to attain more comparable data. Lastly, a test arrangement used to find the best simulation parameters is presented.

Validation of the simulation model is important for obvious reasons: We are after results which give us genuine knowledge about occupational safety in various working conditions and duties performed at electrical substations. The simulations should give consistent results across different kinds of exposure scenarios. The simulation model needs to produce reliable results regardless of the field strength or incident field orientation; the posture of the simulated human model; or the objects and geometries surrounding the body. The resulting absolute internal field values, although important, do not need to be a hundred percent correct. Small errors between the numerical and analytical solutions are acceptable as far greater variation between results is caused by the choice of human phantom model and the conductivity values for different tissue types within.

Conversion from External Field to Internal Field

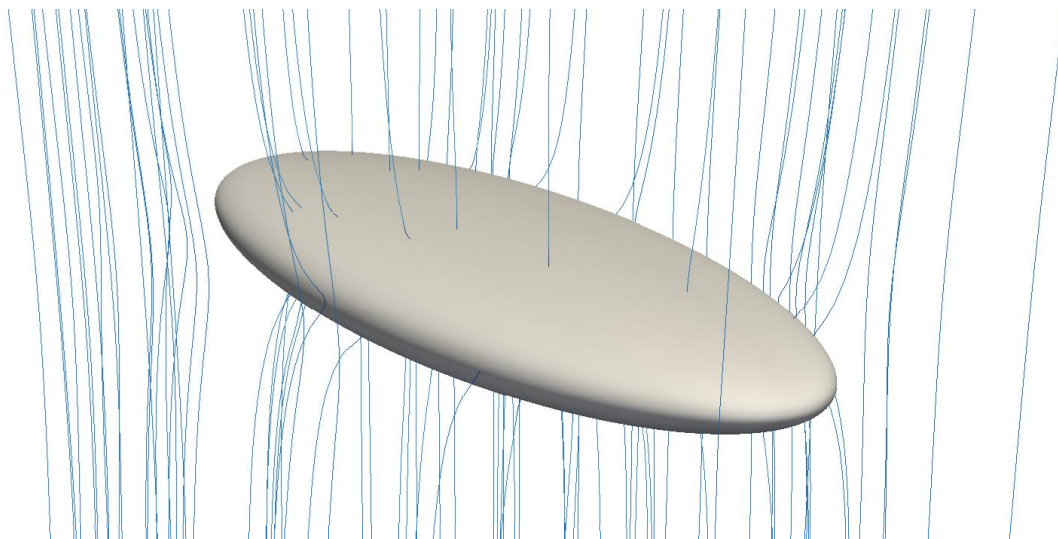


Figure 8: The test object, an ellipsoid, in a 1 kV electric field. The electric field is visualized using streamlines.

The begin with, it was validated that the conversion of the external electric field into current sources on the surface of the body is working as intended, and that the solver for internal electric fields works correctly. To achieve this, it was decided to

use a simplified test scenario where an ellipsoid is standing in a uniform 1 kV/m electric field. The test scenario is visualized in figure 8 above. An ellipsoid is in principle a sphere directionally scaled in all of its three Cartesian coordinates. An ellipsoid was chosen as the test body as it somewhat resembles a standing human. In fact, ellipsoids have historically been used as analogues to human bodies before more accurate human models became available [18]. Additionally, it is possible to analytically calculate the internal electric fields of an ellipsoid. Results of a simulation replicating the analytical scenario can be vetted against this analytical solution to find out how much error our simulation algorithm includes. The ellipsoid chosen to be used in the calculations was 1.75 m tall, 0.6 m wide and 0.2 m thick.

The analytical solution for the electric field inside the ellipsoid was calculated according to the method presented by Juha Avelin in his doctoral dissertation [30]. The internal electric fields for x, y and z-directions are calculated separately using equation (19) with the help of corresponding depolarization factors, equations (20) – (22).

$$E = \frac{\varepsilon_e}{\varepsilon_e + (\varepsilon_i - \varepsilon_e)N_x} E_o \quad (19)$$

$$N_x = \frac{abc}{(a^2 - b^2)\sqrt{a^2 - c^2}} (F(k, \varphi) - E(k, \varphi)) \quad (20)$$

$$N_z = \frac{b}{b^2 - c^2} (b - \frac{ac}{\sqrt{a^2 - c^2}} E(k, \varphi)) \quad (21)$$

$$N_y = 1 - N_x - N_z \quad (22)$$

In these equations a , b and c are the height, width and thickness of the ellipsoid. These measures have to fulfill a condition which states that $a > b > c$. ε_i and ε_e are the internal and external relative permittivities of the ellipsoid. The $F(k, \varphi)$ and $E(k, \varphi)$ in the depolarization factors are incomplete elliptic integrals

$$F(k, \varphi) = \int_0^\varphi \frac{d\psi}{\sqrt{1 - k^2 \sin^2 \psi}} \quad (23)$$

$$E(k, \varphi) = \int_0^\varphi \sqrt{1 - k^2 \sin^2 \psi} d\psi, \quad (24)$$

where

$$k = \sqrt{\frac{a^2 - b^2}{a^2 - c^2}} \quad (25)$$

$$\varphi = \arccos\left(\frac{c}{a}\right). \quad (26)$$

Approximate values for the depolarization factors we used are $N_x \approx 0.05$, $N_y \approx 0.23$ and $N_z \approx 0.72$.

The analytical calculations and simulations were repeated four times using different incident field directions. The field directions studied were: top to bottom, side to side, back to front and a field coming from the top angled at 45° against all three coordinate axes. In addition to the incident field direction, also effects of other simulation parameters, such as the grid size, and size and number of computational domains used, were observed. To assess the quality of the simulations, 99th percentile electric field values for the simulated and analytical solution were calculated and

compared. A 99th percentile value indicates, under what absolute value 99% of all the observed values fall. The main comparison was done by calculating the relative errors between the analytical and numerical solutions.

The direction of the incident field seemed to have a moderate effect on simulation accuracy, as can be seen in table 3. The relative errors between the numerical and analytical solutions were between 1.68 and 5.90% depending of the incident field direction. The relative error was the smallest for the vertical field, and the largest for the horizontally oriented, back to front, electric field. The relative error is the largest for the back to front field because in this scenario the surface area perpendicular to the incident field is the largest. Additionally, this area is relatively flat. When the exposed area of the ellipsoid increases also the errors and artifacts from the staircase approximation begin to accumulate. This increase in relative error should be less pronounced when using a more realistic human body model, with a smaller area and more varied shape.

When the effects of the simulation parameters were observed it was noticed that the grid size used has the largest effect on the simulation accuracy. The simulations were more accurate the smaller the used voxel size was. This can be seen by comparing the relative errors in tables 3 and 4, where results of the simulations utilizing different grid sizes are shown. Hence, the simulations should be run at the smallest possible voxel size, in our case 2 mm. The size of the outermost simulation domain also has a reasonable effect on the simulation accuracy, as is evident when comparing the results in tables 3 and 5, which show simulation results ran using different domain sizes. Increasing the size of the domain only works till a certain point. When the size of the outermost domain is increased, the gained accuracy returns diminish whilst at the same time computational times increase rapidly. Thus, the size of the outer domain should be adjusted carefully to find the best compromise between simulation accuracy and runtime. The number of simulation domains used, had only a minimal effect on the simulation results as long as at least two domains were used: a large domain with plenty of empty space around the ellipsoid and a small domain that barely surrounds the test body. Hereby, the number of nested domains used in the actual simulations can be adjusted according to system resources available and to optimize simulation runtimes without a significant effect on simulation accuracy.

Table 3: Analytically and numerically solved electrical field strengths inside the ellipsoid, relative to each axis. Voxel size used **2 mm** and size of outer most domain $6 \times 6 \times 6 \text{ m}^3$.

Incident field direction	Analytical solution (V/m)			Numerical solution (V/m)			Relative error
	x	y	z	x	y	z	
[1, 0, 0]	19.73	0	0	19.56	1.41×10^{-3}	1.40×10^{-4}	1.68%
[0, 1, 0]	0	4.37	0	1.01×10^{-3}	4.38	1.15×10^{-5}	2.42%
[0, 0, 1]	0	0	1.39	1.94×10^{-4}	-1.34×10^{-5}	1.37	5.90%
[1, 1, 1]	11.39	2.52	0.80	11.29	2.53	0.79	1.76%

Table 4: Analytically and numerically solved electrical field strengths inside the ellipsoid, relative to each axis. Voxel size used **4 mm** and size of outer most domain $6 \times 6 \times 6 \text{ m}^3$.

Incident field direction	Analytical solution (V/m)			Numerical solution (V/m)			Relative error
	x	y	z	x	y	z	
[1, 0, 0]	19.73	0	0	19.58	4.31×10^{-3}	7.31×10^{-4}	2.03%
[0, 1, 0]	0	4.37	0	9.01×10^{-3}	4.39	2.99×10^{-4}	3.00%
[0, 0, 1]	0	0	1.39	2.93×10^{-3}	1.01×10^{-3}	1.37	5.99%
[1, 1, 1]	11.39	2.52	0.80	11.31	2.54	0.79	2.10%

Table 5: Analytically and numerically solved electrical field strengths inside the ellipsoid, relative to each axis. Voxel size used **2 mm** and size of outer most domain $4 \times 4 \times 4 \text{ m}^3$.

Incident field direction	Analytical solution (V/m)			Numerical solution (V/m)			Relative error
	x	y	z	x	y	z	
[1, 0, 0]	19.73	0	0	19.36	1.39×10^{-3}	1.39×10^{-4}	2.32%
[0, 1, 0]	0	4.37	0	9.76×10^{-4}	4.37	9.37×10^{-6}	2.39%
[0, 0, 1]	0	0	1.39	1.88×10^{-4}	-1.48×10^{-5}	1.37	5.91%
[1, 1, 1]	11.39	2.52	0.80	11.18	2.52	0.79	2.35%

Variation Between Phantom Models and a Literature Comparison

Following the successful ellipsoid tests, it was studied how the simulation method performs when realistic voxel based human models are used. A total of five different human models were tested to get an extensive overview of the performance. Three male models: Duke, Norman and Taro, and two female models: Ella and Hanako were used. The same tissue conductivity values as shown in table 2, were used across all body models. Two different electric field exposure scenarios were performed for each model: a grounded and an isolated case. In both scenarios, the model stands upright in a vertical homogeneous 1 kV/m electric field. In the isolated case, the body is surrounded by nothing but air while in the grounded scenario the model stands on a grounded plane with zero potential.

At first, the difference between isolated and grounded scenarios were studied within the same body model. The 99th percentile values of induced electrical field strengths for individual tissues are generally around twice as large for the grounded cases compared with the isolated scenarios. When the whole body 99th percentile field strengths are observed, the difference between the two cases grows. The field strengths in the grounded phantoms are on average six times stronger. Next we studied how much the induced electric field strengths differ from body model to another when the external conditions stay identical. When the induced field values are inspected at tissue level, it becomes obvious that there is considerable variation between the induced field strengths between the phantoms. The standard deviation of internal field strengths for different tissues range from a few percentages all the way to 120% of the mean value. The average deviation between the phantoms is 29%. Thus, comparisons between phantoms on the tissue level are questionable. At the very least, care needs to be taken to only compare values for tissues that demonstrate good consistency across body models. In literature, values for the brain white and grey matter, spinal cord and cerebrospinal fluid are usually reported. These values show reasonable good correlation across body models, with 2–20% variation between the models. When the whole body, 99th percentile field strengths, are compared between phantoms the differences between body models somewhat level out. The variation in the 99th percentile values across the five body models used is on average 28%. It seems that the phantom shape and size affect the induced field strengths in a significant amount. In fact, the variation from body to another is so substantial that it easily conceals the few percentage errors of our simulation method.

As a final validation measure, the internal field strengths produced by our simulations, were compared with values reported in the literature. Only articles that utilized similar test circumstances, 1 kV/m vertical and uniform electric fields, were chosen for comparison. There is no standardized practice on which tissues field strengths are reported for. Nevertheless, almost all publications report electric field strengths for the brain and the spinal cord. Thus, values for these tissues were used in the comparison. The comparative values used were taken from articles written by Dimbylow [19], Hirata [31], Findlay [32] and Magne [33]. These publications cover in total six different body models. All articles studied the phantom models in grounded

conditions while only three had also considered isolated scenarios. It is noteworthy that not all publications used the same tissue conductivity values.

Table 6: Induced field strengths (mV/m) in various grounded phantoms in 1 kV/m, 50 Hz, uniform electric field.

Source	Our simulations					2005 Dimbylow		2010 Hirata		2014 Findlay	2016 Magne	
Phantom model	Norman	Taro	Duke	Hanako	Ella	Norman	Naomi	Taro	Hanako	Maxwell	Taro	Duke
Brain	1.51	1.30	1.21	1.27	1.22	1.65	2.02	1.07	1.12	1.87	1.30	1.80
Spinal cord	3.37	3.19	2.79	2.05	2.27	3.42	2.92	2.18	2.19	3.49	3.40	2.80

Table 7: Induced field strengths (mV/m) in various isolated phantoms in 1 kV/m, 50 Hz, uniform electric field.

Source	Our simulations					2005 Dimbylow		2014 Findlay
Phantom model	Norman	Taro	Duke	Hanako	Ella	Norman	Naomi	Maxwell
Brain	0.90	0.92	0.81	0.88	0.85	0.81	1.22	0.88
Spinal cord	1.66	1.60	1.50	1.18	1.40	1.63	1.40	1.54

As can be seen in tables 6 and 7 there is plenty of variation between the field strengths of different phantom models and even between different simulation methods utilizing the same phantoms. The phantom model Taro, used in our simulations experiences stronger than average internal electric fields compared with the others. This is good for the final simulations as we can be sure that the simulated internal fields are in the stronger end of the spectrum. Altogether, our simulation produces results that are well in line with the ones reported in the literature.

Selection of Simulation Parameters

As previously explained in the simulation algorithm chapter the simulation parameters needed to be carefully chosen to ensure accurate simulation results while retaining simulation performance. The parameters that had the biggest impact on results were the grid size and amount of empty padding in a domain. In an ideal scenario where system memory would be virtually unlimited only one sufficiently large domain utilizing a two-millimeter grid size could be used. Such simulation would require terabytes of system memory and days of precious simulation time. The system used to run our simulations had consumer level hardware and was limited to a total of 64 gigabytes of memory, hence the resources needed to be carefully managed for optimal performance and results. In the outermost domain where a large volume is necessary the voxel grid size needs to be scaled in proportion to conserve system memory. Respectively, it is possible to use a small voxel size in the smallest domain due to the small volume. Multiple combinations of a simulation volumes and grid sizes were tested to find a combination producing the most accurate field strength results.

The testing was carried out using a test scenario where an electrically charged finite length wire crosses the simulation domain. The test scenario was run with 240 different combinations of grid sizes and domain volumes to find the parameters producing the best results. The wire used in the calculations and simulations had the same radius, potential and height from the ground as the main electric field sources, the busbars, in the real simulation scenarios. When the wire is long, field calculations can be carried out as if the wire was infinitively long. Thus, the electric field of the wire is only dependent of the perpendicular distance from the wire. The electric field produced by such wire running over a grounded plane can be analytically solved using the 2D method of image charges. The method of image charges states that the electric field of a charged particle on top of a conductive plane is equal to a scenario, where two opposite charged particles are in a vacuum at double the distance the original particle is from the ground plane. The electric field strength at point \mathbf{r} from the wire is given by equation (27). The charge of a particle representing a part of the wire is calculated from equation (28) using the potential U , the radius R , and height from the ground h of the real busbar.

$$E = \frac{Q}{2\pi\epsilon_0|\mathbf{r}|} \quad (27)$$

$$Q \approx \frac{U \times 2\pi\epsilon_0}{\ln(R) - \ln(2 \times h - R)} \quad (28)$$

The electric fields produced by the two opposite charged 2D particles are calculated separately and summed together to obtain the total electric field. The analytical solution was calculated for over 4 million points around the wire. The electric fields for the same points were also calculated using the simulation algorithm, and finally a relative error between the two fields was calculated.

A part of the calculated relative errors are presented in table 8. The smallest relative error was achieved using an outer domain with forty meters of padding, combined with a grid size of nine centimeters. The parameters for the middle

domain were five meters and four centimeters respectively. A simulation using these parameters resulted in an electric field with a relative error of 5.2% compared with the analytical solution. The general trend in getting the most accurate results was to use the largest possible simulation volume, while at the same time keeping the voxel size at a scale that enables the geometry to be reproduced accurately. Having a smaller voxel size does not necessary result in better object reproduction when the objects to be reproduced and the voxel size are close to each other. Such is the case for example here: The wire with a diameter of 10 cm is more accurately portrayed by 9 cm voxels than slightly smaller 8.8 cm ones.

Table 8: Relative error between the analytical and numerical solution, with different voxel and padding sizes. The grayed out region indicates insufficient system memory.

Padding (m)	Voxel size (cm)				
	8.6	8.8	9	9.2	9.4
25	...	10.10%	7.98%	8.58%	...
26	...	14.28%	7.65%	8.24%	...
27	...	6.85%	7.34%	17.80%	...
28	...	6.58%	7.07%	7.67%	...
29	...	15.89%	6.83%	7.43%	...
30	...	8.75%	6.61%	7.20%	...
31	...	8.55%	13.57%	7.01%	...
32	...	8.37%	13.38%	6.83%	...
33	...	8.21%	6.06%	9.36%	...
34	...	8.06%	5.91%	6.50%	...
35	...	7.93%	5.77%	6.36%	...
36	...	7.80%	5.63%	6.23%	...
37	...	14.52%	5.51%	6.11%	...
38	...	7.58%	5.40%	6.00%	...
39	...	7.48%	5.30%	5.90%	...
40	5.22%	5.81%	...
41	5.72%	∴
42
43
44

5 Results

In this chapter results of the field measurements as well as the simulations will be presented.

Results of Experimental Measurements

As previously described, a number of different experimental measurements were conducted at an electric substation. The measurements were conducted to get reference values that can later be compared with simulation results. The data from these measurements is presented here in this chapter. Also the results derived are presented. The first measurement conducted involved general mapping of electric field strengths around the circuit breaker at the height of 1.7 meters. The measured field strengths are shown in figure 9. As can be seen from the figure, the electric fields surrounding the circuit breakers are clearly strong enough to exceed the low 10 kV ALs. Thus, studying the electric fields induced in human bodies when exposed to these fields is necessary to ensure that working conditions stay safe. Another observation that can be made about the external field is that it seems to be stronger close to conductive structures, and the fields seem to intensify towards the gap between the cophasal busbars.

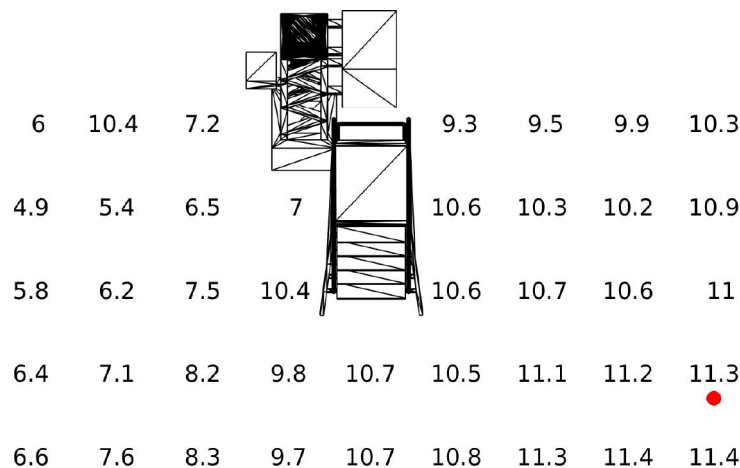


Figure 9: Measured field strengths in kV/m. The red dot indicates the location of the field strength measurement at 3.5 m height.

In addition to the general electric field strength mapping, single measurements were performed at various locations. Results of these field strength measurements are listed in table 9 below. From the table it can be seen that the external fields get stronger the higher you get off the ground level, or the closer you get to conductive objects. The geometry can also act as a partial Faraday cage, weakening electric fields locally, as can be seen from the measurements conducted at different heights off the service platform. The measurement point beneath the railing level (1.16 m), shows that the geometry can have a significant effect on field strengths. Another example of the geometry working as cover against the strongest fields is the scenario

where the control unit cabin door is open. When the door is open it partially covers from the electric flux flowing from the side.

Table 9: Electric field strengths at various locations.

Location / Height (m)	Measured external \mathbf{E} (kV/m)			
	Middle of service platform	Back end of service platform Door closed	Door open	Between cophasal busbars
3.05	-	-	-	12.6
1.7	18.6	20.3	18.5	-
1.5	17.7	16.5	-	-
1.16	11.1	9.4	-	-

In addition to, the external field strength measurements, currents induced into a test subject's body were measured using the helmet-mask measurement system. The raw data of these current measurements is shown in figure 10. The subject moved between measurement locations, shown in figure 14, and stood still at each location for a short while, so that around half a minute of data was gathered for each specific location. The measurement locations and respective approximate time points are: Standing in front of the service platform (0–20 s), standing on the service platform (25–55 s), standing on the service platform with the control unit cabin door open (70–100 s), standing underneath the cophasal busbars (150–200 s), standing in front of the current transformer (215–240 s), and lastly standing on the right side of the service platform (275–300 s).

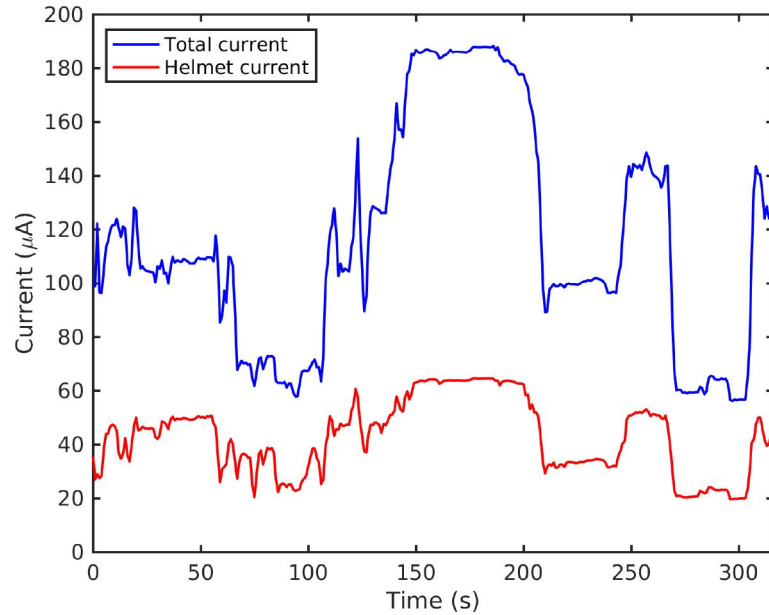


Figure 10: Induced currents measured with the helmet-mask measurement system.

The average and maximum currents for each location were calculated and are presented in table 10. Also calculated estimates of induced internal field strengths are shown. The estimates were calculated using formula (1). The measured currents

seem to be nicely in line with the measurement location external field strengths. The largest currents are induced in locations with the strongest external field strengths. Also, the effect of the surrounding geometry is visible on the current measures. For example, having the door open leads to smaller measured current values. Similarly, the calculated internal electric field strengths are in relation with the external field strengths and measured currents.

Table 10: Current measures done using the helmet-mask measurement system and internal electric fields calculated from the maxima.

	Measured currents (μA)				Calculated internal \mathbf{E} from maximum values (mV/m) RMS
	Average		Max		
	Neck	Total	Neck	Total	
Platform (door closed)	45.6	106.0	50.7	117.8	42.6
Platform (door open)	30.2	66.8	38.7	72.8	32.6
Under cophasal busbars	63.4	184.0	64.5	188.3	54.3
In front of stairs	40.1	112.0	41.0	113.1	34.5
Next to stairs	21.4	60.3	24.0	65.5	20.2
Current transformer	33.3	99.8	34.6	101.9	29.1

As the last measurement, the disruption of the external field caused by a human body was studied. The field strengths measured by the electric ELF field probe are plotted in figure 11 together with field strengths from the simulations. The two graphs are not completely comparable as the external electric field strength at the measurement location were not equal to begin with. Still, the figure shows how the field strengths grow in a similar fashion when the human body gets closer to the measurement point.

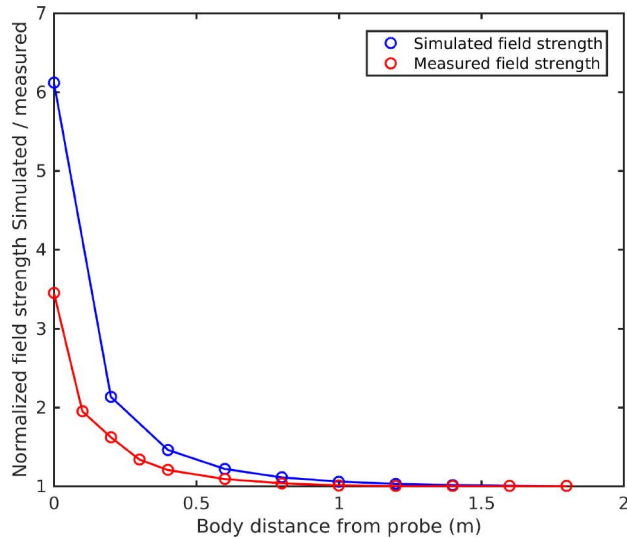


Figure 11: Distruption of the external field when the human body approaches the measurement probe. The field strengths are normalized.

Simulation Results

The main objective of the computational simulations is to investigate if the EU directive ELVs are exceeded at the study site. Additionally, there is interest in verifying that the helmet-mask measurements previously conducted by Fingrid produce reliable results. To achieve these goals, a number of simulation scenarios utilizing the Taro human phantom model were conducted. The scenarios were kept similar to the helmet-mask measurements performed at the substation so that a reliable comparison between the two can be made. A secondary goal for the simulations is to acquire a general image of the electric fields and their behavior at the test site. To accomplish this secondary goal, the simulated external electric fields are visualized and the results analyzed. The electric field strengths from this overview simulation scenario can be directly compared with the measured data. This way it is possible to verify that the simulations produce results true to life. For this overview simulation, no phantoms were positioned into the geometry. This was done to eliminate any disruptions caused to the external fields by a conductive body.

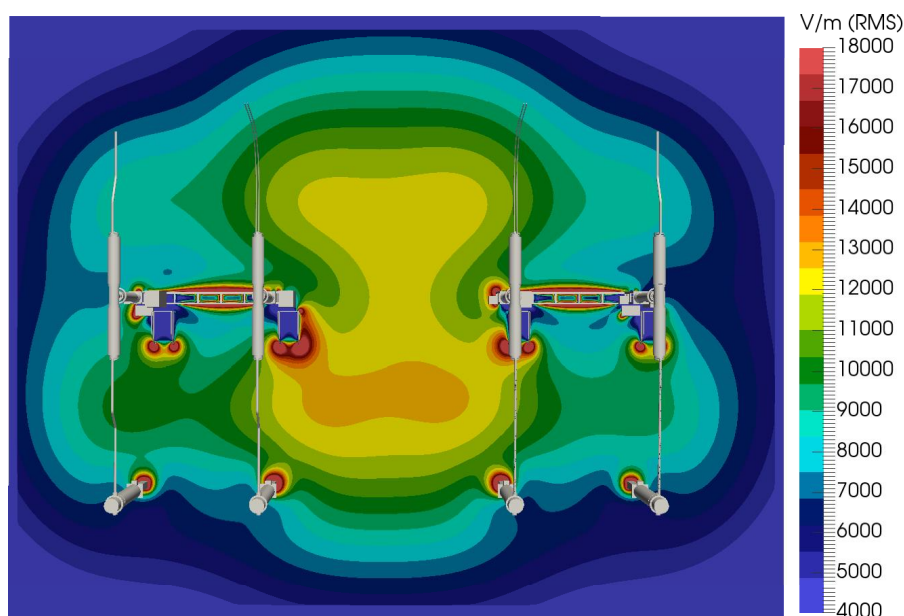
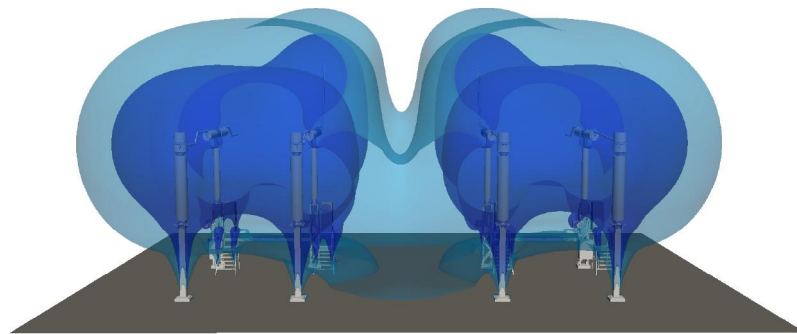


Figure 12: Simulated electric field strengths at head level (1.7 m).

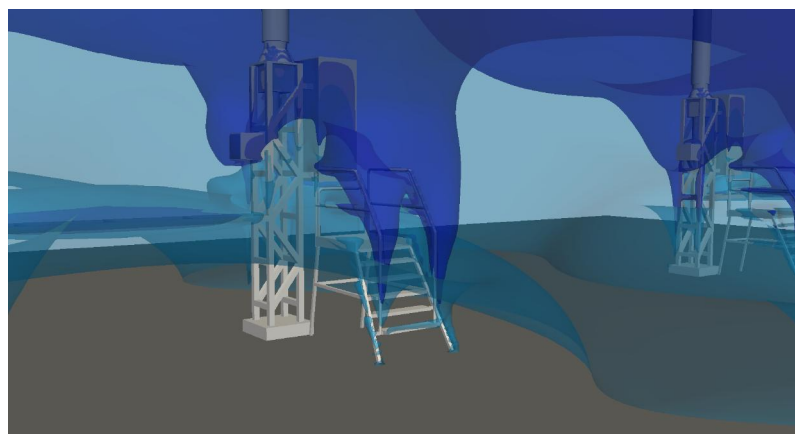
To begin with, a general look at the electric field strengths in the simulation domain will be taken. Figure 12 presents a contour of the field strengths at head level, 1.7 meters up from the ground plane. The electric fields are at their strongest, right next to conductive objects, such as the aluminum staircases leading to the service platform, and close to the metallic structural pillars of the circuit breakers and current transformers. It is also obvious from the contour plot that strong electric fields reside between the two middle cophasal busbars. The ALs imposed by the 2010 EU directive are clearly exceeded near the circuit breakers. The field strength values of the simulations are in line with previous studies performed by Fingrid. In their studies, the strongest fields have been pinpointed to the gap between the

cophasal circuit breakers, like in the simulations. The simulated field strengths also match the measurements reported in the previous chapter. When the simulated electric field strengths are interpolated to the exact locations used as test points during the experimental measurements, it is evident that the fields are alike although the simulated electric fields are on average 28% stronger. The simulated electric fields appear stronger than the measured fields because of the voxelization of the geometry. The voxelization increases volumes of some objects, especially the volumes of the narrow busbars. This enlargement of the electric field sources strengthens the external electric field.

To visualize the electric fields around the geometry even better, images of the volumetric 3D data were rendered. Figure 13 shows an overview representing where the thresholds for the ALs are located and a close up of the thresholds on the service platform. The volumetric renders reveal nicely how the electric fields are distributed around the geometry, how the fields concentrate near conductive objects, as well as where the geometry acts as protection, creating pockets where the field strengths are weaker. For example, the railings around the service platform function as a partial Faraday cage, greatly weakening the fields on the platform. Occurrences like this can have large effects on the fields induced to the human body, as will be seen later on in the chapter.



(a) Overview of the simulation domain.



(b) Close up of the circuit breaker service platform.

Figure 13: 10 kV/m and 20 kV/m electric field strength thresholds.

Now that an overview of the simulated external electric fields has been established, the next step will be to analyze the simulations utilizing the Taro human phantom model. A total of twelve different simulations, studying the induction of currents and electric fields into the phantoms, were performed. Six of these simulations attempt to replicate the helmet-mask current measurements described earlier in this thesis. In these scenarios, the phantom is grounded through a 10×15 cm electrode attached to the left forearm of the phantom. In this scenario, the currents flowing through the electrode and the neck of the phantom are solved. The other six simulations are run to solve the induced electric field strengths in the phantom while standing at various locations and when electrically isolated from the surroundings.

The previously described simulations utilizing the phantoms were repeated in five different locations within the geometry. These five locations are: Firstly, the human phantom standing on the circuit breaker service platform, with both the control unit cabin door open and closed; secondly, the phantom standing in front of and next to the service platform; thirdly, the phantom standing next to the current transformer; and lastly a setting where the phantom is positioned underneath the cophasal busbars. The exact positioning of the phantoms within the geometry is shown in figure 14 below. By conducting these twelve simulations, it is possible to both confirm if the EU directive ELVs are exceeded and if the helmet-mask current measurements are reliable.

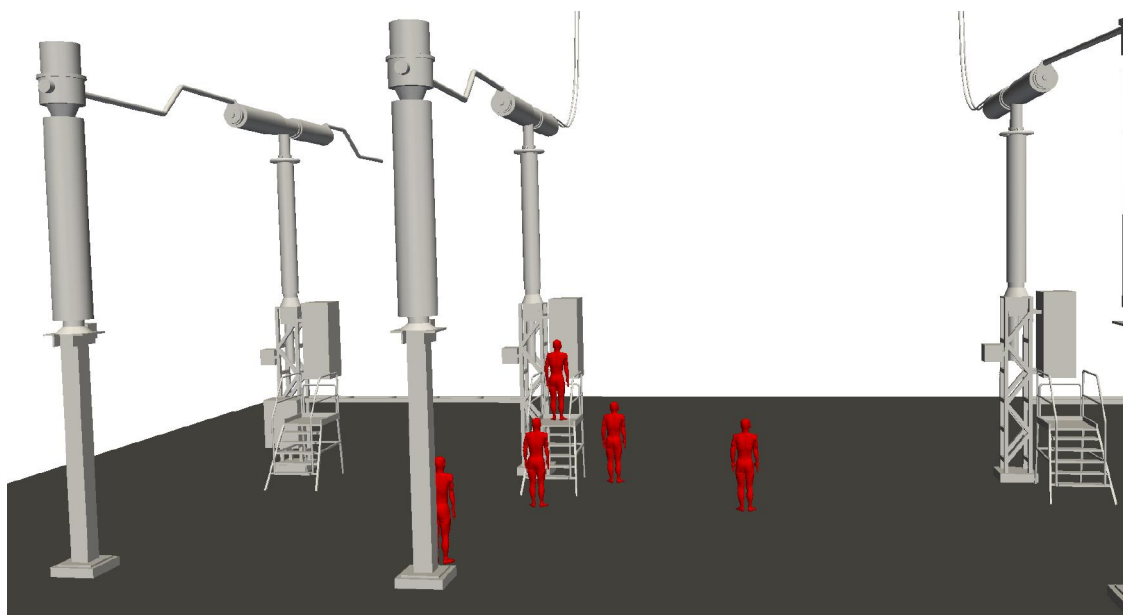


Figure 14: Phantom locations during internal electric field simulations.

The simulation results are presented in figures 15 through 26 and in tables 11 & 12. The figures portray how the induced electric fields are distributed across the phantoms in different settings. In all of the twelve figures, the phantom is portrayed with the internal electric field strengths projected onto it. Additionally, graphs showing the 99.9th percentile field strength values for each transverse plane of the phantom have been drawn. The blue curve takes into account the whole body while

the red curve only includes the data points in the torso and head of the phantom. The limbs have been separated from the torso to give a better picture of the field strength distribution between the hands and the trunk of the phantom. It is important to realize that the values shown in the graphs are not comparable with the safety limits imposed by the EU directive. The graphs are strictly for visualizing the distribution of field strengths within the phantoms. The values in the graphs are not comparable with the EU safety limits, because the percentile values are calculated from separate transverse planes and not from the whole body or CNS. Calculating the percentile from a single plane results in a larger field strength. When direct comparisons between the simulated internal field strengths and EU safety limits are wanted, the values presented in the two tables should be used instead.

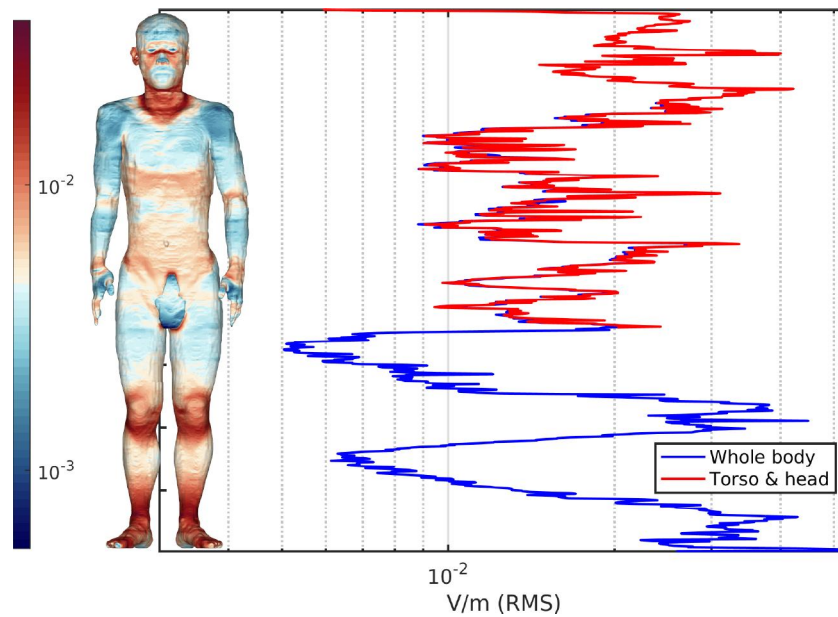


Figure 15: Internal electric field strengths (untreated data on phantom, 99.9th percentiles in graph) on **service platform, door closed, ungrounded**.

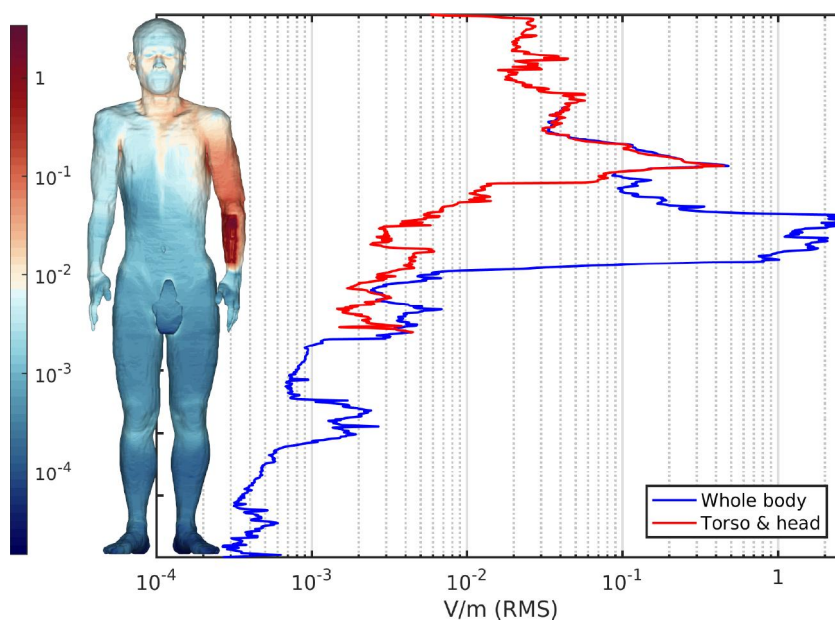


Figure 16: Internal electric field strengths (untreated data on phantom, 99.9th percentiles in graph) on **service platform, door closed and electrode attached**.

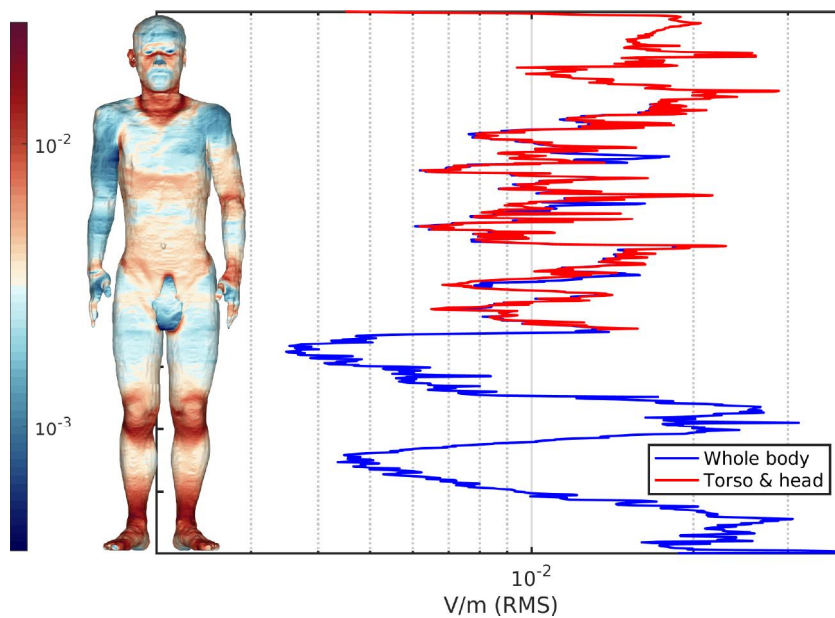


Figure 17: Internal electric field strengths (untreated data on phantom, 99.9th percentiles in graph) on **service platform, door open, ungrounded**.

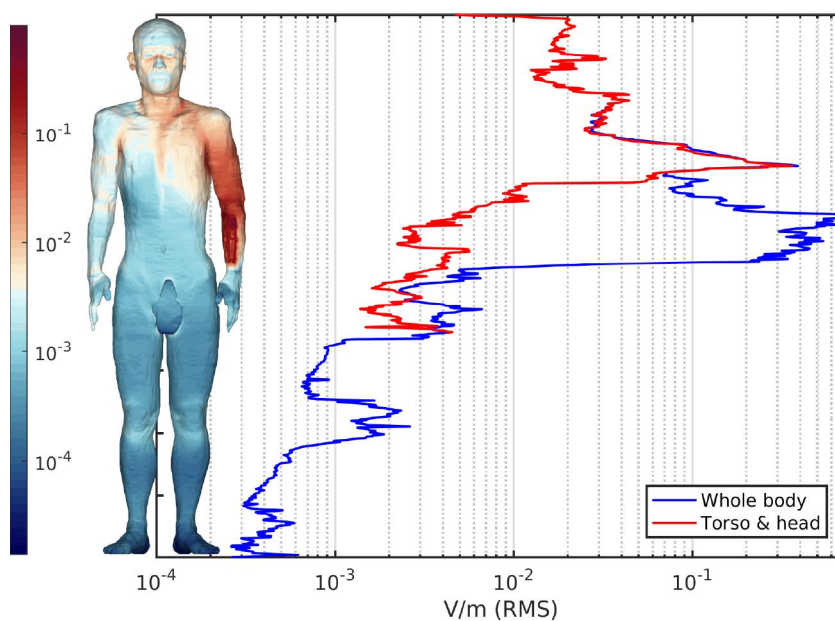


Figure 18: Internal electric field strengths (untreated data on phantom, 99.9th percentiles in graph) on **service platform, door open and electrode attached**.

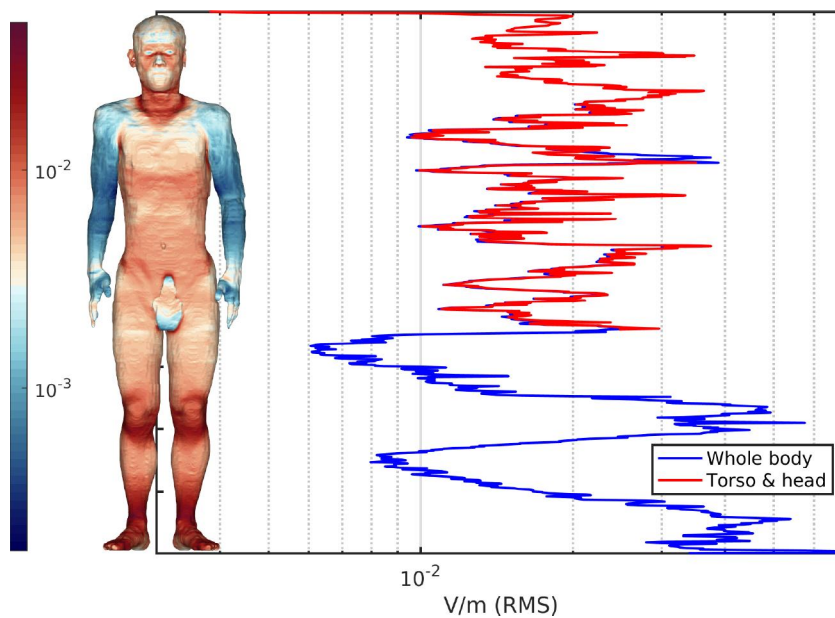


Figure 19: Internal electric field strengths (untreated data on phantom, 99.9th percentiles in graph) **under cophasal busbars, ungrounded**.

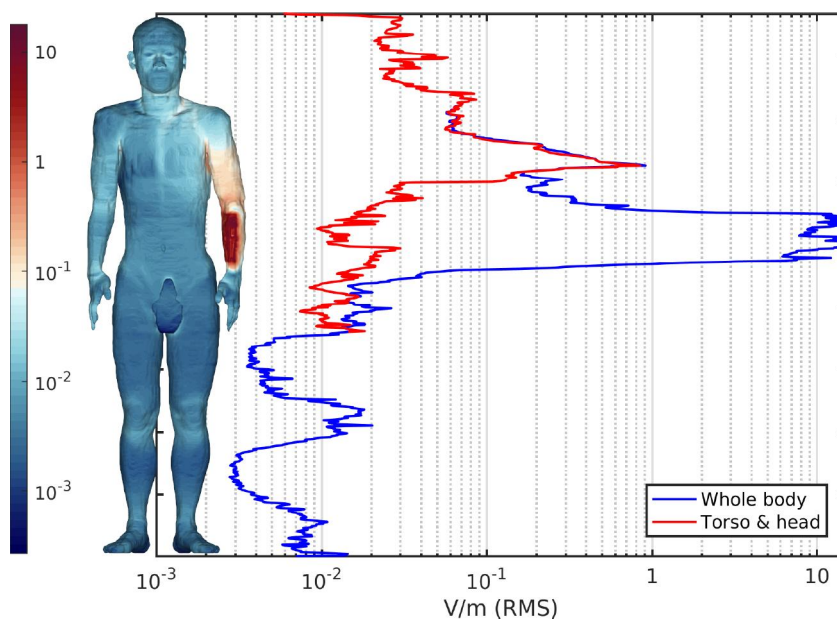


Figure 20: Internal electric field strengths (untreated data on phantom, 99.9th percentiles in graph) **under cophasal busbars, electrode attached.**

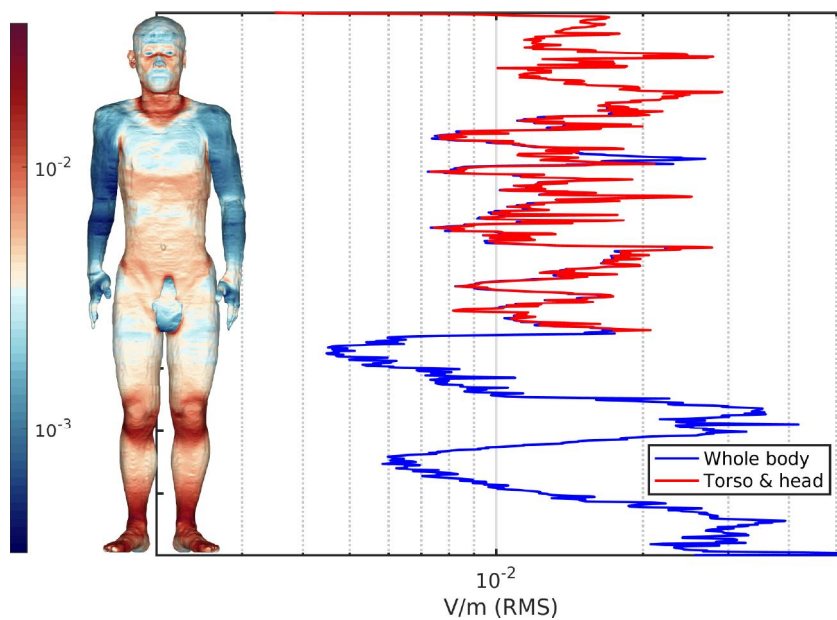


Figure 21: Internal electric field strengths (untreated data on phantom, 99.9th percentiles in graph) **in front of service platform, ungrounded.**

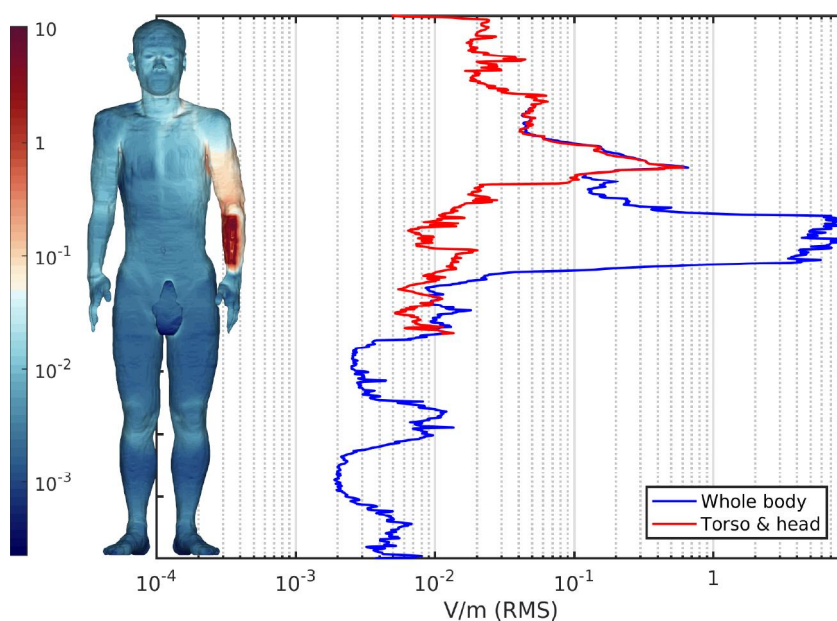


Figure 22: Internal electric field strengths (untreated data on phantom, 99.9th percentiles in graph) **in front of service platform, electrode attached.**

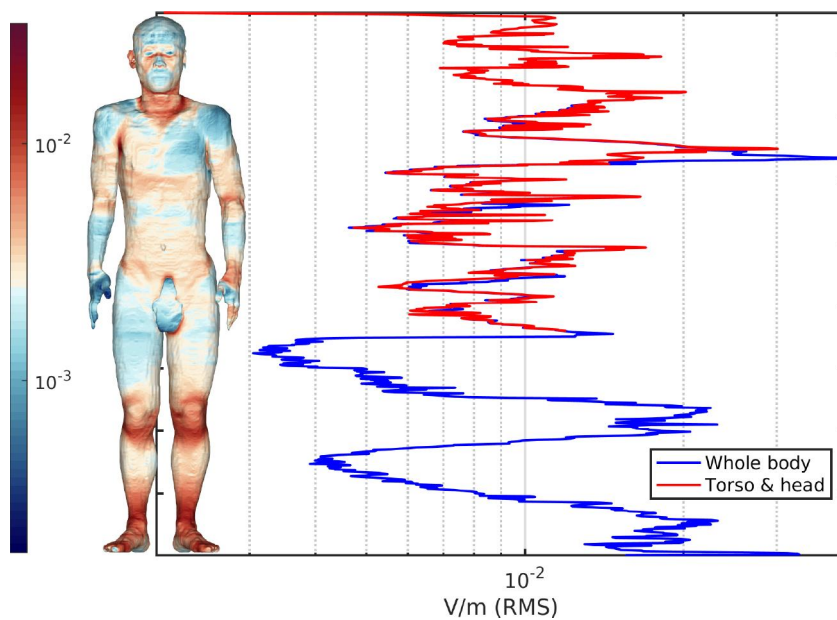


Figure 23: Internal electric field strengths (untreated data on phantom, 99.9th percentiles in graph) **next to service platform, ungrounded.**

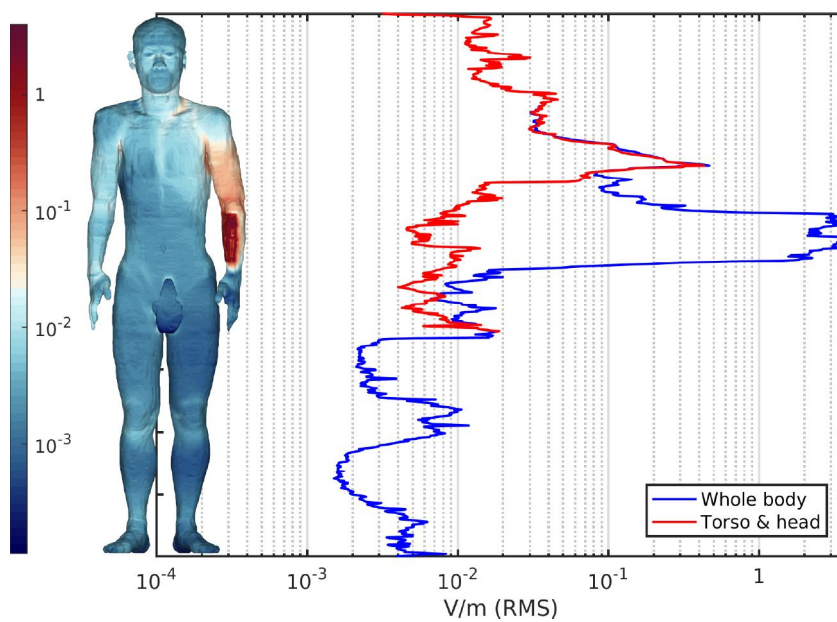


Figure 24: Internal electric field strengths (untreated data on phantom, 99.9th percentiles in graph) next to service platform, electrode attached.

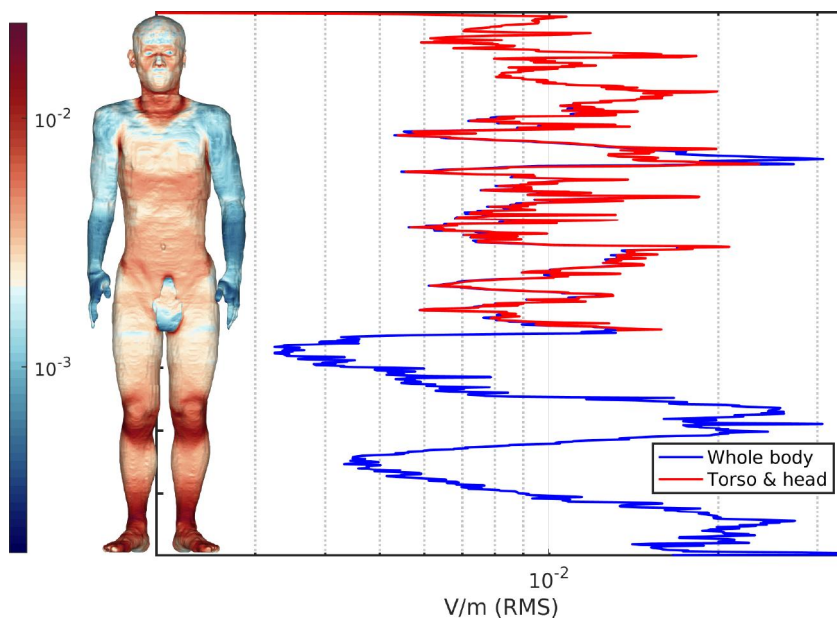


Figure 25: Internal electric field strengths (untreated data on phantom, 99.9th percentiles in graph) next to current transformer, ungrounded.

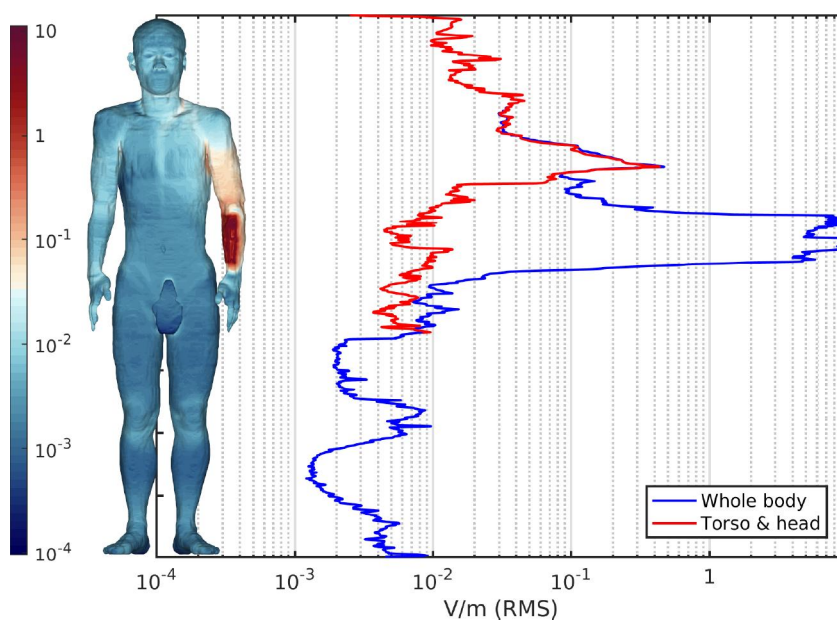


Figure 26: Internal electric field strengths (untreated data on phantom, 99.9th percentiles in graph) next to current transformer, electrode attached.

From the above figures it can be observed that the electric field distributions within the phantoms changes drastically depending if the phantom is grounded or not. The largest field strengths in the grounded phantoms can be over ten times stronger than in the isolated cases. The field strengths in the grounded conditions increase across the spectrum, and especially in the arm the electrode is attached to. This is simply explained by the larger potential difference between the body and its surroundings. The strong internal field strengths in the arms are explained by the fact that all the induced currents flowing through the arm towards the electrode and ground potential.

The surrounding geometry seems to have a noticeable effect on the field distributions as well, at least in the isolated scenarios. In the grounded scenarios, the influence of the grounding electrode trumps over any effects of the surrounding geometry. The effects of the surroundings are best seen when comparing the graphs of a phantom standing on the service platform, figure 15 and a phantom standing underneath the parallel busbars, figure 19. The field strengths in the legs are proportionally weaker in the legs when the phantom is standing on the service platform. It is probable that this is due to the platform guard railings somewhat shielding the lower body from the external field. The effect of surroundings is also visible between the scenarios where the control unit cabin door is closed and open, figures 15 and 17. When the door is open, it attracts the bulk of the electric flux while the human body receives less exposure compared with the case with the door being closed.

When comparing the torso only and whole body graphs with each other it is obvious that the arm with the electrode attached to it experiences the strongest internal field strengths. This occurs because all currents being induced to the body flow through this hand with relatively little cross-section area. It seems that the internal field strengths in the arms get so strong that it could be possible for the EU safety limits to be exceeded locally.

In tables 11 & 12 the maximum internal electric field strengths are listed for both isolated and grounded cases. The field strengths were averaged over each tissue type and the maximum value corresponding to the whole body or the CNS only, is reported. This representation is as per the Non-binding guide to good practice for implementing Directive 2013/35/EU by the European Commission [23]. In addition to the maximum value, the corresponding tissue type is specified. The simulations indicate that the strongest internal electric fields occur at tissues with low conductivities, such as the bones, fat tissue and the brain white matter. Strong fields also occur in higher conductivity tissues such as tendons, in congested regions of the body such as the ankles and knees. In addition to the previously reported values, 99.9th percentile values calculated over the whole body and torso are also reported. These values can be used as additional reference. The tables also include simulated and measured external field strength values at each phantom location, as well as simulated currents comparable to the ones measured with the helmet-mask measurement system.

The results in the second and fourth columns in table 11 can be directly compared with the 2010 EU directive ELVs, table 1. Neither the limits for health or sensory

effects are exceeded in these isolated scenarios. The induced electric field strengths are on average 3% of the health effect limit and 10% of the sensory effect limit. Even in the worst case scenario, where the phantom is standing either beneath the cophasal busbars or on the circuit breaker service platform with the control unit cabin door closed, the respective percentages are 4% and 15%. Hereby, the safety limits are no where close to being exceeded. The sixfold safety margin is enough to cover all inaccuracies in the simulations, as well as any variation possibly caused by slightly different geometries, phantom sizes as well as phantom postures. The 99.9th percentile values for the whole body and the torso are in line with the tissue specific 99th percentile values. The safety limits are not exceeded.

The results, in table 12, portray the induced field strengths while wearing the helmet-mask measurement system. The results indicate that the internal field strengths are notably higher than in the isolated exposure scenarios. The induced electric field strengths are on average 18% of the health ELV and 14% of the sensory effect ELV. In the worst case, under the cophasal busbars, the percentages are 33% and 20%. Thus, the safety limits remain untouched. The 99.9th percentile values indicate that it might be possible that the internal field strengths exceed the EU limits locally. However, the strongest 0.1% values, can also contain erroneous data points.

Table 11: Simulation results for isolated phantom model. RMS values.

	Max \mathbf{E} (mV/m) in a single tissue, 99th percentile	Tissue	Max \mathbf{E} (mV/m), CNS tissue, 99th percentile	Tissue	Max \mathbf{E} (mV/m), whole body, 99.9th percentile	Max \mathbf{E} (mV/m), torso & head, 99.9th percentile	Field strength at location, head level (kV/m)	
							Simulated	Measured
Platform (door closed)	25.85	Tendon	14.65	White matter	26.46	24.63	19.4	20.3
Platform (door open)	18.39	Tendon	9.87	White matter	18.69	17.22	19.2	18.5
Under cophasal sub bars	32.54	Tendon	12.15	White matter	32.37	22.06	12.4	10.7
In front of stairs	23.71	Tendon	10.06	White matter	23.87	17.36	12.8	10.6
Next to stairs	14.74	Tendon	6.44	White matter	15.44	12.75	11.0	9.0
Current transformer	16.80	Tendon	6.43	White matter	17.03	12.11	12.4	11.3

Table 12: Simulation results for grounded phantom model. RMS values.

	Max \mathbf{E} (mV/m) in a single tissue, 99th percentile	Tissue	Max \mathbf{E} (mV/m), CNS tissue, 99th percentile	Tissue	Max \mathbf{E} (mV/m), whole body, 99.9th percentile	Max \mathbf{E} (mV/m), torso & head, 99.9th percentile	Neck current (μA)	Total current μA
Platform (door open)	79.79	Cancellous bone and bone marrow	11.67	White matter	133.01	86.39	29.0	77.2
Under cophasal sub bars	254.38	Cortical bone	19.81	White matter	1048.92	202.43	51.2	184.4
In front of stairs	168.03	Cortical bone	15.42	White matter	610.65	145.94	39.2	132.4
Next to stairs	102.80	Cancellous bone and bone marrow	10.36	White matter	255.23	103.94	26.5	90.7
Current transformer	144.68	Cortical bone	10.49	White matter	657.52	104.25	27.3	95.5

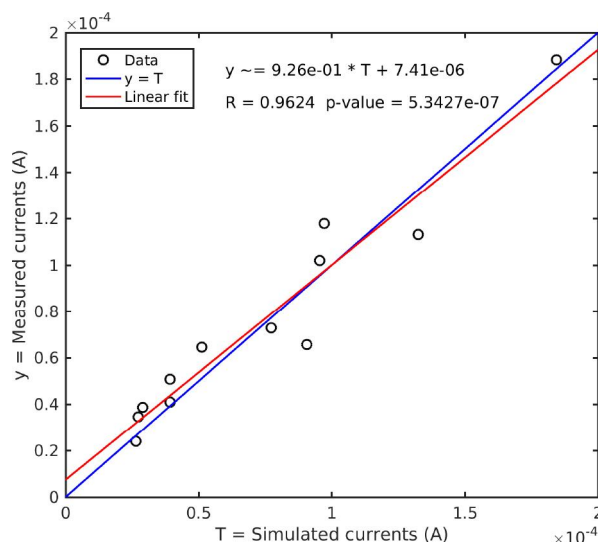
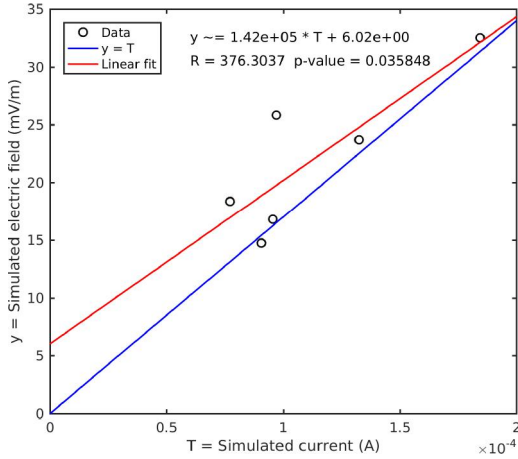


Figure 27: Correlation between experimentally measured and simulated currents.

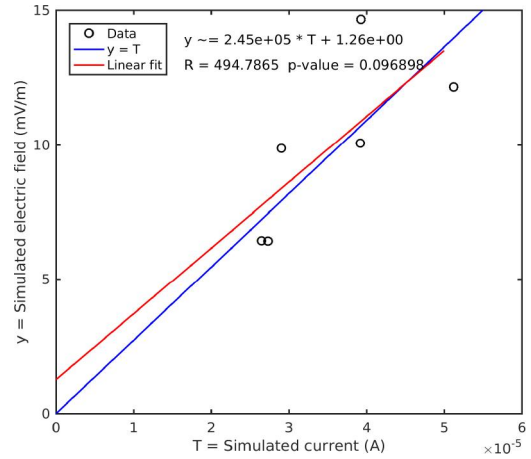
After being shown that occupational work, in the surroundings of the circuit breakers, does not expose workers to induced electric fields exceeding the EU safety limits, we will move on to examine how the helmet-mask measurements correspond with the simulated results. Figure 27 shows the results of a regression analysis performed on the measured currents in table 10 and simulated currents in table 11. From the graph, it is obvious that the measured and simulated results correlate strongly with each other. The helmet-mask measurement system seems to produce reliable data about the induced internal currents.

The next logical question is, how well does the measured currents represent the induced internal field strengths? To get an answer to this question, regression analysis between the simulated currents and internal field results were run. The results of these analyses indicate that the total and neck currents, measured using the helmet-mask measurement system, correlate with the induced field strengths in the grounded scenarios. This fact is visible in figures 29a and 29b. In the isolated cases, correlation is certain only between the total current and the maximum tissue specific field strength in the whole body. This fact can be observed from the regression plots in figures 28a and 28b. In the light of these findings, it should be possible to calculate the internal field strength values using a mathematical model. Fingrid has previously used the simplified equation (2), which they have formulated in collaboration with Tarao et al. to calculate induced field strengths. The equation has been reported to work well, for the CNS. To confirm this, another set of regression analyses were run, this time between the simulated internal field strengths and the field strengths calculated using the simplified equation. The results of these analyses can be seen in figures 30a, 30b, 31a and 31b. There is obvious correlation between the calculated and simulated internal field strengths in the isolated case as well as in the grounded case for the CNS. For the grounded whole body scenario, correlation can not be confirmed. It is noteworthy that the sample size for each regression analysis was only six data points. Thus, further experimental measurements and simulations could be performed to attain a greater certainty about correlation. It is also entirely possible

that the grounded whole body scenario with plenty of uncertainty could show more probable correlation. From the studies completed so far it can be concluded that the simplified equation works at calculating the internal field strengths in the isolated scenario and in the CNS when the body is grounded through the other forearm.

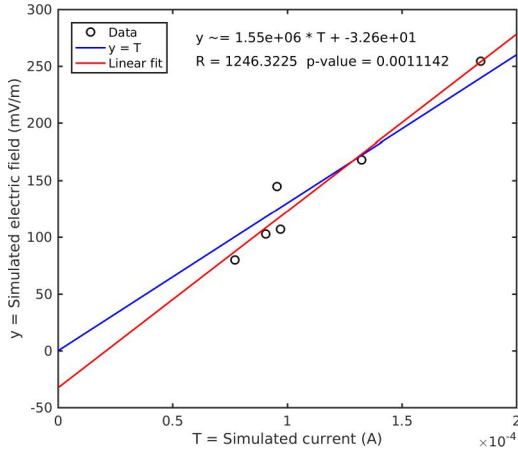


(a) Max \mathbf{E} in single tissue against **total current**.

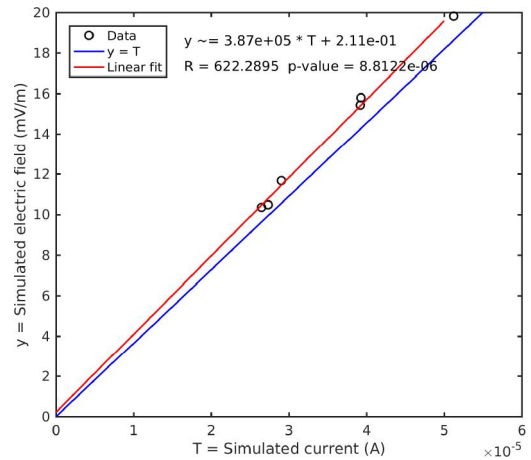


(b) Max \mathbf{E} in the CNS against **neck current**.

Figure 28: Regression analysis between simulated currents and simulated internal electric fields, in the **isolated** scenario.



(a) Max \mathbf{E} in single tissue against **total current**.



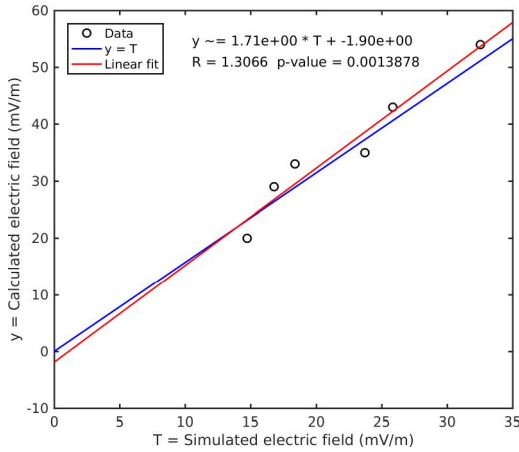
(b) Max \mathbf{E} in the CNS against **neck current**.

Figure 29: Regression analysis between simulated currents and simulated internal electric fields, in the **grounded** scenario.

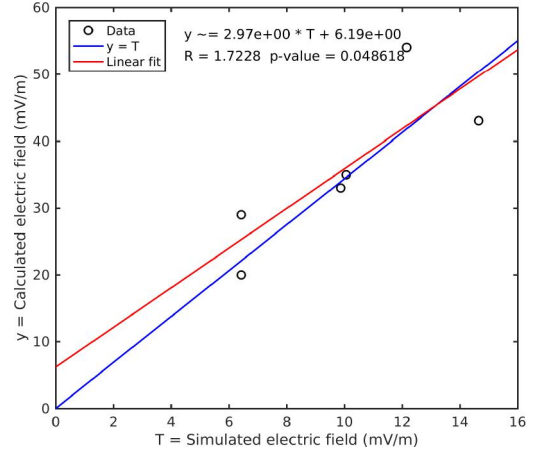
Although, the simplified equation did not work for the grounded whole body scenario, an empirical mathematical model can be created from the correlation between the total current and the maximum field strength in the whole body. This model is presented in equation (29). This model is created from only six data

points and it can be further improved by increasing the sample size by running more simulations and performing comparative measurements. The required sample size is determined by how small of a confidence interval is deemed necessary for the model.

$$E_{tot} = 1.3 \times 10^6 \times I_{tot} \quad (29)$$

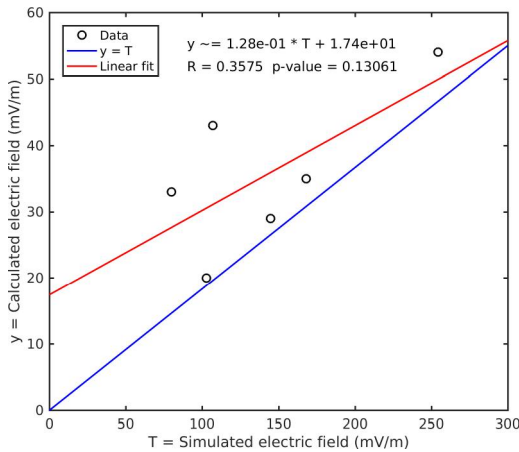


(a) Calculated \mathbf{E} against max \mathbf{E} in **single tissue**.

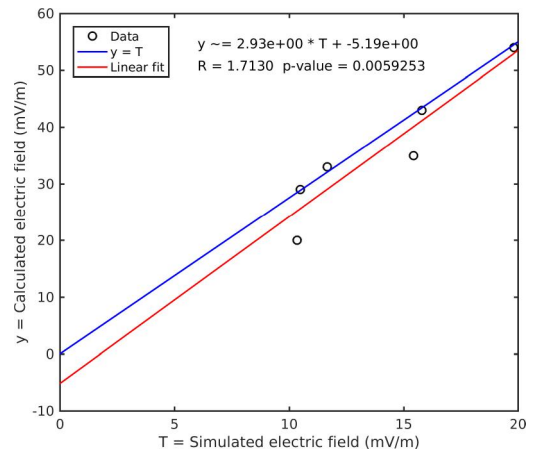


(b) Calculated \mathbf{E} against max \mathbf{E} in the **CNS**.

Figure 30: Regression analysis between simulated internal electric fields and calculated electric fields using the simplified equation, in the **isolated** scenario.



(a) Calculated \mathbf{E} against max \mathbf{E} in **single tissue**.



(b) Calculated \mathbf{E} against max \mathbf{E} in the **CNS**.

Figure 31: Regression analysis between simulated internal electric fields and calculated electric fields using the simplified equation, in the **grounded** scenario.

6 Conclusions

When the work on this thesis began a number of goals to be achieved were set. The goals set were to study if the 2013 EU directive safety limits for electric field exposure are exceeded when performing occupational work tasks at an electrical substation, specifically in the vicinity of circuit breakers; does the helmet-mask measurement system produce accurate results; can these current measurement results be reliably converted into representing induced internal field strengths using a simplified equation; and lastly, to visualize the induced internal as well as the external electric fields at the site of research. All of these goals have been met in the work.

The results of the thesis work are in summary as follows: according to the simulations, the external electric fields are at their strongest between the cophasal busbars and close to any conductive grounded objects. Both the low and high EU directive ALs are exceeded locally at the study site. Thus, the internal field strengths being induced into the human body need to be studied to verify occupational safety. The simulated external field strengths are on average 28% stronger than the measured field strengths. This difference can be looked as a positive thing, as solving the induced internal field strengths from a slightly stronger external field generates some extra safety margin. The cause of the stronger external field strengths is the voxelization of the geometry, which leads to larger volume busbars and thus in larger volume electric field sources.

The simulated results utilizing the Japanese Taro phantom model indicate that the induced internal field strengths do not exceed the EU directive safety limits. On average, the induced field strengths are 3% of the health effects limit and 10% of the sensory effects limit in the isolated scenarios. In the grounded cases, the respective percentages are 4% and 15%. In the very worst scenario, where a grounded human is standing underneath the two cophasal busbars, there is a threefold safety margin between the induced field strengths and the safety limits. This margin should be enough to account for any simulation errors or variations caused by the size, shape or posture of the human phantom model. The strongest field strengths are induced into tissues with low electrical conductivity values, such as cortical and cancellous bone, bone marrow and fat tissue. Strong field strengths also occur in tissues with higher conductivities if located in narrow areas of the body such as the knees and ankles. This is due to currents flowing through the body concentrating at these locations with small cross sectional areas. When studied field strengths are limited into tissues in the CNS the strongest fields occur in the brain white matter.

The results of the performance analysis between the helmet-mask measurement system and the simulations indicate that the measurement system produces reliable results. The simplified equation used to calculate the internal field strengths produces consistent results that are in line with the simulations in all but one scenario. In the single case where the simple equation does not hold true, it is proposed that an empirical equation formulated and presented in this thesis is used instead. The similarity between the measured and simulated results also validates our numerical model.

Altogether, the work concluded in this thesis can be regarded as a success. The

work is a first of its kind to demonstrate that electric fields can be simulated at an accurate level in a large scale realistic environment. The work also holds some future potential, as the developed software can easily be adapted to simulate electric fields at other environments and locations.

References

- [1] The European Parliament and the council of the European Union, “Directive 2013/35/EU of the European Parliament and of the council,” *Official Journal of the European Union*, vol. 56, pp. 1–21, 2013. [Online]. Available: <http://eur-lex.europa.eu/legal-content/EN/TXT/?uri=celex:32013L0035>
- [2] —, “Directive 2004/40/EC of the European Parliament and of the council,” *Official Journal of the European Union*, vol. 47, pp. 1–9, 2004. [Online]. Available: <http://eur-lex.europa.eu/legal-content/EN/TXT/?uri=CELEX:32004L0040>
- [3] ICNIRP, “Guidelines for limiting exposure to time-varying electric and magnetic fields (1 Hz to 100 kHz),” *Health Phys*, vol. 99, no. 6, pp. 818–36, 2010. [Online]. Available: <http://www.icnirp.de/documents/LFgdl.pdf>
- [4] World Health Organization, “Non-ionizing radiation, part 1: Static and extremely low-frequency (ELF) electric and magnetic fields,” *IARC Monographs on the Evaluation of Carcinogenic Risks to Humans*, 2002. [Online]. Available: <http://monographs.iarc.fr/ENG/Monographs/vol80/mono80.pdf>
- [5] J. Latva-Teikari, T. Karjanlahti, J. Kurikka-Oja, J. Elovaara, T. Långsjö, and L. Korpinen, “Measuring occupational exposure to electric and magnetic fields at 400 kV substations,” 2008. [Online]. Available: <http://ieeexplore.ieee.org/document/4517068/>
- [6] L. Korpinen, J. Elovaara, and H. A. Kuisti, “Evaluation of current densities and total contact currents in occupational exposure at 400 kV substations and power lines,” *Bioelectromagnetics*, vol. 30, pp. 231–240, 2009. [Online]. Available: <http://onlinelibrary.wiley.com/doi/10.1002/bem.20468/full>
- [7] L. Korpinen, H. Kuisti, R. Pääkkönen, P. Vanhala, and J. Elovaara, “Occupational exposure to electric and magnetic fields while working at switching and transforming stations of 110 kV,” *The Annals of Occupational Hygiene*, vol. 55, pp. 526–536, 2011. [Online]. Available: <https://academic.oup.com/annweh/article/55/5/526/158801>
- [8] L. Korpinen, H. A. Kuisti, H. Tarao, and J. Elovaara, “Occupational exposure to electric fields and currents associated with 110 kV substation tasks,” *Bioelectromagnetics*, vol. 33, pp. 438–442, 2012. [Online]. Available: <http://onlinelibrary.wiley.com/doi/10.1002/bem.21711/full>
- [9] L. Korpinen and R. Pääkkönen, “Occupational exposure to electric and magnetic fields during tasks at ground or floor level at 110 kV substations in Finland,” *International Journal of Occupational Safety and Ergonomics*, vol. 22, pp. 384–388, 2016. [Online]. Available: <http://www.tandfonline.com/doi/abs/10.1080/10803548.2016.1153858>

- [10] L. Korpinen, J. Elovaara, and H. A. Kuisti, “Occupational exposure to electric fields and induced currents associated with 400 kV substation tasks from different service platforms,” *Bioelectromagnetics*, vol. 32, pp. 79–83, 2011. [Online]. Available: <http://onlinelibrary.wiley.com/doi/10.1002/bem.20612/full>
- [11] L. Korpinen, H. A. Kuisti, and J. Elovaara, “Current densities and total contact currents for 110 and 220 kV power line tasks,” *Bioelectromagnetics*, vol. 35, pp. 531–535, 2014. [Online]. Available: <http://onlinelibrary.wiley.com/doi/10.1002/bem.21870/full>
- [12] H. Tarao, H. Kuisti, L. Korpinen, N. Hayashi, and K. Isaka, “Effects of tissue conductivity and electrode area on internal electric fields in a numerical human model for ELF contact current exposures,” *Phys Med Biol*, vol. 57, pp. 2981–2996, 2012. [Online]. Available: <http://iopscience.iop.org/article/10.1088/0031-9155/57/10/2981/meta>
- [13] H. Tarao, L. Korpinen, H. Kuisti, N. Hayashi, J. Elovaara, and K. Isaka, “Numerical evaluation of currents induced in a worker by ELF non-uniform electric fields in high-voltage substations and comparison with experimental results,” *Bioelectromagnetics*, vol. 34, pp. 61–73, 2013. [Online]. Available: <http://onlinelibrary.wiley.com/doi/10.1002/bem.21738/full>
- [14] H. Tarao, H. Miyamoto, L. Korpinen, N. Hayashi, and K. Isaka, “Simple estimation of induced electric fields in nervous system tissues for human exposure to non-uniform electric fields at power frequency,” *Phys Med Biol*, vol. 61, pp. 4438–4451, 2016. [Online]. Available: <http://iopscience.iop.org/article/10.1088/0031-9155/61/12/4438/meta>
- [15] P. J. Dimbylow, “FDTD calculations of the whole-body averaged SAR in an anatomically realistic voxel model of the human body from 1 MHz to 1 GHz,” *Phys Med Biol*, vol. 42, pp. 479–90, 1997. [Online]. Available: <http://dx.doi.org/10.1088/0031-9155/42/3/003>
- [16] —, “Induced current densities from low-frequency magnetic fields in a 2 mm resolution, anatomically realistic model of the body,” *Phys Med Biol*, vol. 43, no. 2, pp. 221–30, 1998. [Online]. Available: <http://stacks.iop.org/0031-9155/43/221>
- [17] —, “Current densities in a 2 mm resolution anatomically realistic model of the body induced by low frequency electric fields,” *Phys Med Biol*, vol. 45, no. 4, pp. 1013–22, 2000. [Online]. Available: <http://stacks.iop.org/0031-9155/45/1013>
- [18] ICNIRP, “Guidelines for limiting exposure to time-varying electric, magnetic and electromagnetic fields (up to 300 GHz),” *Health Phys*, vol. 74, no. 4, pp. 492–522, 1998. [Online]. Available: <http://www.icnirp.de/documents/emfgdl.pdf>
- [19] P. J. Dimbylow, “Development of the female voxel phantom, NAOMI, and its application to calculations of induced current densities and

- electric fields from applied low frequency magnetic and electric fields,” *Phys Med Biol*, vol. 50, no. 6, pp. 1047–70, 2005. [Online]. Available: <http://stacks.iop.org/0031-9155/50/i=6/a=002>
- [20] ———, “Development of pregnant female, hybrid voxel-mathematical models and their application to the dosimetry of applied magnetic and electric fields at 50 Hz,” *Phys Med Biol*, vol. 51, no. 10, pp. 2383–94, 2006. [Online]. Available: <http://stacks.iop.org/0031-9155/51/2383>
- [21] R. P. Findlay and P. J. Dimbylow, “Effects of posture on FDTD calculations of specific absorption rate in a voxel model of the human body,” *Phys Med Biol*, vol. 50, no. 16, pp. 3825–35, 2005. [Online]. Available: <http://stacks.iop.org/0031-9155/50/i=16/a=011>
- [22] P. Dimbylow and R. Findlay, “The effects of body posture, anatomy, age and pregnancy on the calculation of induced current densities at 50 Hz,” *Radiat Prot Dosimetry*, vol. 139, no. 4, pp. 532–8, 2010. [Online]. Available: <http://rpd.oxfordjournals.org/content/139/4/532.abstract>
- [23] European Commission, “Non-binding guide to good practice for implementing directive 2013/35/EU,” 2015. [Online]. Available: <https://publications.europa.eu/en/publication-detail/-/publication/c6440d35-8775-11e5-b8b7-01aa75ed71a1>
- [24] X. G. Xu and K. F. Eckerman, *Handbook of Anatomical Models for Radiation Dosimetry*. Florida, USA: Taylor & Francis, 2009.
- [25] T. Nagaoka, S. Watanabe, K. Sakurai, E. Kunieda, S. Watanabe, M. Taki, and Y. Yamanaka, “Development of realistic high-resolution whole-body voxel models of Japanese adult males and females of average height and weight, and application of models to radio-frequency electromagnetic-field dosimetry,” *Phys Med Biol*, vol. 49, no. 1, pp. 1–15, 2004. [Online]. Available: <http://stacks.iop.org/0031-9155/49/1>
- [26] S. Gabriel, R. W. Lau, and C. Gabriel, “The dielectric properties of biological tissues: III. Parametric models for the dielectric spectrum of tissues,” *Phys Med Biol*, vol. 41, no. 11, pp. 2271–93, November 1996. [Online]. Available: <http://stacks.iop.org/0031-9155/41/2271>
- [27] ———, “The dielectric properties of biological tissues: II. Measurements in the frequency range 10 Hz to 20 GHz,” *Phys Med Biol*, vol. 41, no. 11, pp. 2251–69, 1996. [Online]. Available: <http://stacks.iop.org/0031-9155/41/2251>
- [28] A. Christ, W. Kainz, E. G. Hahn, K. Honegger, M. Zefferer, E. Neufeld, W. Rascher, R. Janka, W. Bautz, J. Chen, B. Kiefer, P. Schmitt, H.-P. Hollenbach, J. Shen, M. Oberle, D. Szczerba, A. Kam, J. W. Guag, and N. Kuster, “The Virtual Family—development of surface-based anatomical models of two adults and two children for dosimetric simulations,” *Phys Med Biol*, vol. 55, no. 2, pp. N23–38, 2010. [Online]. Available: <http://stacks.iop.org/0031-9155/55/i=2/a=N01>

- [29] I. Laakso and A. Hirata, “Fast multigrid-based computation of the induced electric field for transcranial magnetic stimulation,” *Phys Med Biol*, vol. 57, no. 23, pp. 7753–65, 2012. [Online]. Available: <http://stacks.iop.org/0031-9155/57/i=23/a=7753>
- [30] J. Avelin, “Polarizability analysis of canonical dielectric and bi-anisotropic scatterers,” *Electromagnetics Laboratory report series*, no. 414, 2003. [Online]. Available: <https://aaltodoc.aalto.fi/handle/123456789/2148>
- [31] A. Hirata, Y. Takano, Y. Kamimura, and O. Fujiwara, “Effect of the averaging volume and algorithm on the in situ electric field for uniform electric- and magnetic-field exposures,” *Phys Med Biol*, vol. 55, no. 9, pp. N243–52, 2010. [Online]. Available: <http://stacks.iop.org/0031-9155/55/i=9/a=N03>
- [32] R. P. Findlay, “Induced electric fields in the MAXWEL surface-based human model from exposure to external low frequency electric fields,” *Radiation Protection Dosimetry*, vol. 162, pp. 244–253, 2014. [Online]. Available: <https://academic.oup.com/rpd/article/162/3/244/1607587>
- [33] I. Magne and F. Deschamps, “Electric field induced in the human body by uniform 50 Hz electric or magnetic fields: bibliography analysis and method for conservatively deriving measurable limits,” *Journal of Radiological Protection*, vol. 36, pp. 419–436, 2016. [Online]. Available: <http://iopscience.iop.org/article/10.1088/0952-4746/36/3/419/meta>